ANL-22/48

Design Methods, Tools, and Data for Ceramic Solar Receivers Year 1 Continuation Report

---

Applied Materials Division

About Argonne National Laboratory

Argonne is a U.S. Department of Energy laboratory managed by UChicago Argonne, LLC under contract DE-AC02-06CH11357. The Laboratory's main facility is outside Chicago, at 9700 South Cass Avenue, Lemont, Illinois 60439. For information about Argonne and its pioneering science and technology programs, see www.anl.gov.

DOCUMENT AVAILABILITY

Online Access: U.S. Department of Energy (DOE) reports produced after 1991 and a growing number of pre-1991 documents are available free at OSTI.GOV (http://www.osti.gov/), a service of the US Dept. of Energy's Office of Scientific and Technical Information.

Reports not in digital format may be purchased by the public from the National Technical Information Service (NTIS):

U.S. Department of Commerce
National Technical Information Service
5301 Shawnee Rd
Alexandria, VA 22312
www.ntis.gov
Phone: (800) 553-NTIS (6847) or (703) 605-6000
Fax: (703) 605-6900
Email: **orders@ntis.gov**

Reports not in digital format are available to DOE and DOE contractors from the Office of Scientific and Technical Information (OSTI):

U.S. Department of Energy
Office of Scientific and Technical Information
P.O. Box 62
Oak Ridge, TN 37831-0062
www.osti.gov
Phone: (865) 576-8401
Fax: (865) 576-5728
Email: **reports@osti.gov**

Disclaimer

This report was prepared as an account of work sponsored by an agency of the United States Government. Neither the United States Government nor any agency thereof, nor UChicago Argonne, LLC, nor any of their employees or officers, makes any warranty, express or implied, or assumes any legal liability or responsibility for the accuracy, completeness, or usefulness of any information, apparatus, product, or process disclosed, or represents that its use would not infringe privately owned rights. Reference herein to any specific commercial product, process, or service by trade name, trademark, manufacturer, or otherwise, does not necessarily constitute or imply its endorsement, recommendation, or favoring by the United States Government or any agency thereof. The views and opinions of document authors expressed herein do not necessarily state or reflect those of the United States Government or any agency thereof, Argonne National Laboratory, or UChicago Argonne, LLC.

ANL/22-48

Design Methods, Tools, and Data for Ceramic Solar Receivers Year 1 Continuation Report

---

prepared by
Pawan Chaugule
Dileep Singh
Bipul Barua
Mark C. Messner

Applied Materials Division, Argonne National Laboratory

August 2022

ABSTRACT

This report describes the first year of work on a project to develop the methods, tools, and data required to analyze high temperature ceramic Concentrating Solar Power (CSP) components. This first year focused on developing the methods and data required for a time-independent assessment of potential components, focusing in particular on ceramic solar receivers. The report describes both model development and testing work focused on accomplishing this goal. Our overall conclusion is that high temperature ceramic CSP components are viable and could provide a means to overcome the expected low reliability and short service life for equivalent components constructed from Ni-based superalloys. Based on the results reported here, we recommend the project continue to Phase II which will develop more sophisticated, realistic models for time-dependent failure of ceramics operating in expected CSP component conditions and develop the time-dependent ceramic test data needed to parameterize these models, using commercial SiC as a reference material.

TABLE OF CONTENTS

Abstract i
Table of Contents iii
List of Figures v
List of Tables vi
1 Introduction 1
2 Implementation and Verification of Time-independent Ceramic Failure Models 5
  2.1 Principle of Independent Action (PIA) 5
  2.2 Weibull Normal Stress Averaging (WNSA) 6
  2.3 Crack shape dependent models 6
  2.4 Verification 11
  2.5 Summary and discussion 16
3 High Temperature Ceramic Material Data 18
  3.1 Overview 18
  3.2 Experimental results 18
  3.3 Processing the data 20
  3.4 MAX phase test data 23
4 Thermohydraulic Solver for Tubular Panel Receivers 25
  4.1 Thermohydraulic solver procedure 27
  4.2 Validating the thermohydraulic solver 29
  4.3 Fluid thermal properties 29
5 Assessing the Viability of Ceramic Receivers 33
  5.1 Reference receiver 33
  5.2 Thermohydraulic analysis 34
  5.3 Structural analysis 35
  5.4 Reliability analysis 36
  5.5 Comparison with metallic receivers 40
6 Conclusions 42
Acknowledgements 43
Bibliography 44

LIST OF FIGURES

Figure 1.1. Illustration of how time-dependent flaw growth will affect the strength of ceramic materials. 2
Figure 2.1. Flow chart of time independent failure models implemented in *srlife*.. 5
Figure 2.2. Direction cosines l, m and n of the stress tensor σ in principal stress space. 8
Figure 2.3. (a) Polar plot of solid angle Ω containing all crack normals for which effective stress > critical stress. (b) Polar plot showing the effective stress/normal stress for all the models presented in Chapter 3, with respect to the critical stress. GF denotes Griffith crack/flaw and PSF denotes penny shaped crack/flaw. 11
Figure 2.4. Pressurized disk experimental test. 12
Figure 2.6. (a) Geometry, loading, and boundary condition (b) quarter symmetry 3D finite element model, and (c) example results from structural analysis of the transversely loaded circular disc example provided in CARES/LIFE manual [3]. 12
Figure 2.7. Comparison of failure probabilities from CARES manual (symbols) and srlife, generated using the models (a) PIA, WNTSA, MTS, CSE, and SMM for penny-shaped flaw and (b) MTS, CSE and SMM for Griffith flaw. 15
Figure 2.8. Comparison of failure probabilities predicted from all the models implemented in srlife, with the experimental data from Rufin and Bollard [16]. 16
Figure 3.1. Configuration of four-point bend test where L = 40 mm. 18
Figure 3.2. Flexure strength (MPa) vs density (g/cc) from high temperature tests on SiC commercial grade. 19
Figure 3.3. Comparison of flexure strength (MPa) data from current experiments on commercial SiC and literature values on α- SiC [21]. 20
Figure 3.4. Failure probability plots for SiC (commercial grade) at (a) room temperature (b) high temperature (750° C). 22
Figure 3.5. Cumulative probability distribution plots for SiC (commercial) using (left) characteristic strength σθ and (right) scale parameter σ0 i.e. for unit volume. 23
Figure 3.6. Plot of flexure strength (MPa) data from current experiments and literature values from MAX Phase of different phase contents (%) and grain structure. 24
Figure 4.1. Simplified panel flow path model used in the thermohydraulic solver. 25
Figure 5.1. (a) Heat flux map on the reference receiver at noon. Numbers 1 to 6 indicates the panels in the receiver along two flow paths. (b) Heat flux variation during the day. 33
Figure 5.2. (a) Variation in fluid mass flow rate, optimized to achieve nearly constant, 720°C outlet temperature. (b) Changes in fluid and tube crown temperatures (shown for two representative tubes per panel considered in simulation) along the flow path from the start of the day to noon. (c) Tube outer wall temperature distribution (shown for Tube-1) at noon. Results are from thermohydraulic analysis of the reference receiver considering SiC as the tube material and for 1 mm thick tubes. Numbers 1 to 6 indicates the panels in the receiver along two flow paths. 34
Figure 5.3. Stress distributions (shown for Tube-1) at noon. Results are from structural analysis of the reference receiver considering SiC as the tube material and for 1 mm thick tubes. Numbers 1 to 6 indicates the panels in the receiver along two flow paths. 36
Figure 5.4. Individual tube reliabilities of the reference receiver using PIA model. Tube material: SiC (literature) and tube thickness: 1 mm. 37
Figure 5.5. Minimum tube reliability vs ceramic failure model. Tube material: SiC (literature) and tube thickness: 1 mm. 38
Figure 5.6. Minimum tube reliability vs tube thickness. Tube material: SiC (literature). 39
Figure 5.7. Minimum tube reliability vs tube material. Tube thickness: 3 mm. The bar for SiC (tested) is not visible because tube reliability for this material is about zero for all the models. 40

LIST OF TABLES

Table 2.1. Comparison between probability of failure values obtained from PIA and WNTSA models for different mixed stresses. 14
Table 3.1. Average dimensions of samples........ 18
Table 3.2. Summary of tests conducted, and results obtained. 19
Table 3.3. Weibull distribution parameter estimates for SiC (commercial grade). 22
Table 3.4. Summary of tests conducted on MAX Phase material. 23
Table 4.1. Properties of chloride salt (32% MgCl2 / 68% KCl). Valid for temperature between 723K to 1073K. 31
Table 4.2. Isobaric properties of sCO_2. Valid for temperature between 600K to 1050K. 31
Table 4.3. Values of the coefficients in Table 4.2. 31
Table 5.1. Material parameters used in reliability analysis. 37
Table 5.2. Comparison between metallic and ceramic receivers. 41

1 Introduction

The outlet temperature targets for Gen 3 Concentrating Solar Power (CSP) systems will challenge the structural reliability of high temperature metallic materials [1-2]. Moreover, looking ahead, process heat requirements to decarbonize industrial processes such as steel and ammonia production will require even hotter outlet temperatures [3-4]. Therefore, alternative materials should be considered for future CSP systems.

Advanced ceramics are a promising material system [5]. This class of materials has excellent high temperature strength and relatively low thermal expansion. Current challenges include the limited ductility of some materials as well as fabrication and joining ceramics both to themselves and to other plant components.

However, before addressing the manufacturing challenges, first CSP developers will need to determine if high temperature ceramic components are a potentially viable in the context of a complete system design. The plant operating life is one key factor in assessing the economics of an operating system. As such, system developers need a way to assess the expected operating life of ceramic components under the challenging high temperature service conditions that will be found in next-generation CSP systems. An accurate tool for estimating the life of ceramic components will allow developers to:

1. Assess the basic viability of ceramic components by comparing equivalent ceramic and metallic component designs.
2. Compare different ceramic materials based on cost and expected operating life.
3. Make accurate cost projections for systems including ceramic components.

This report describes the first year of progress building, testing, and validating a life estimation tool for ceramic components for high temperature concentrating solar power systems. We implemented the tool as an extension to *srlife* – an open-source software package for evaluating the life of high temperature metallic CSP components [6].

One key difference between our past work on the life of high temperature metallic components and the current work on ceramics is that there is considerably more variability in the high temperature strength of ceramics than there is in metallic materials. Given this variability, ceramic life estimation, both at low and elevated temperatures, is typically statistical. That is, rather than provide an estimate of the expected service life of a component, the target for a ceramic would be the probability distribution that a given components can survive a given loading for a given period of time. The design metric would then be the combination of a desired service life, say 30 years, and a required reliability, i.e., the goal is to design a component to last a given amount of time with a target reliability.

The work to date represents a partial step towards a complete high temperature statistical analysis package aimed at calculating this type of design metric for a ceramic CSP component. Specifically, the work to date has focused on time-independent failure in ceramic materials. The standard view of ceramic failure is that the material, in the as-manufactured condition, has a microscale distribution of flaws. This flaw distribution is inherent to the material, in the sense of both the particular composition and the processing used to form that material into the component or sample. Time-independent failure models calculate the probability that a given state of stress at the macroscale will cause the critical flaw in this distribution to grow unstably, i.e., in the sense of fast, brittle fracture. A variety of theories exist for evaluating this probability. We implemented many of the most common failure theories, relying on prior aerospace experiments, particularly at NASA [7], working with ceramic components.

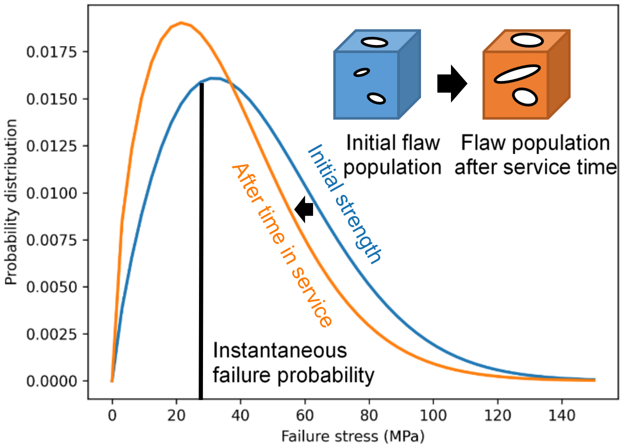

Figure 1.1. Illustration of how time-dependent flaw growth will affect the strength of ceramic materials.

However, time-independent failure models of this type only tell part of the story. In long-term high temperature service crack growth mechanisms like creep, fatigue, and creep-fatigue will alter the initial, as-manufactured flaw distribution. The time-independent failure models we implemented in this performance period will then need to be supplemented with models for how the initial flaw distribution grows as a function of time, stress, temperature, and other relevant environmental factors. Developing models of this type and collecting the requisite experimental data will be the main focus of the second year of the project.

In this first year the project accomplished several key research and development goals:

1. We implemented and validated a library of time-independent ceramic failure models, based on prior NASA experience working with high temperature ceramics. These models and a general high temperature ceramic analysis module have been added to the open-source *srlife* software (Chapter 2).

2. We collected bend test data from samples of a commercial SiC ceramic. This test data was then processed to create the material models needed to execute a time-independent statistical analysis of high temperature CSP components. In addition, we collected additional failure data and corresponding failure models using SiC data from the literature and using data on MAX phase composites, collected as part of another project. These data sources allow us to assess the life of high temperature CSP components made from several different advanced engineering ceramics, as well as to assess the effect of material processing on the strength and reliability of SiC (Chapter 3).
3. We implemented a simple thermohydraulic simulation capability in *srlife*. This simulation capability replaces the previous model of relying on outside software to conduct the thermohydraulic system analysis, prior to the built-in thermal and structural solvers in *srlife* being used to determine the temperature and stress fields in the component itself. This task was not part of the original project scope. However, we found that integrating the thermohydraulic analysis into *srlife* greatly simplified the process of comparing CSP receiver designs using widely different materials (i.e., metals and ceramics). A fair comparison between material systems for the same receiver design would target the same inlet and outlet coolant temperatures given the same incident flux distributions, which, for materials with different thermal properties, does not mean the same tube wall thickness. This new solver greatly simplifies the process of making fair comparisons for receivers manufactured from different materials (Chapter 4).
4. Finally, we used the new time-independent ceramic assessment capabilities to assess the viability of Gen 3 tubular receivers manufactured from advanced engineering ceramics. We compared designs using SiC (both our heat and another commercial heat from literature data) and MAX phase materials to a variety of equivalent metallic designs. These calculations demonstrate the basic viability of ceramic high temperature receivers, in particular those constructed using commercial SiC. MAX phase materials are also promising, but obtaining the required material samples for time-dependent testing may be difficult and there is currently significantly batch-to-batch variation in the MAX phase material failure data (Chapter 5).

In addition, a long-lead time order was placed on a creep test system capable of time-dependent bend testing. This system will be a key piece of equipment for gathering time-dependent failure data on ceramic materials to support time-dependent statistical failure models.

Finally, Chapter 6 summarizes our conclusions and recommendations. In brief, these are:

- High temperature ceramic CSP receivers are viable competitors when compared to metallic designs. Metallic molten salt or sCO2 receivers operating in Gen III conditions have very short service lives. Ceramic materials, at least analysed using time-independent failure models, could be viable for long-term service.
- We recommend continuing the test campaign to collected time-dependent material data on commercial SiC material. This material is the most likely near-term engineering ceramic that could be applied to high temperature CSP systems. MAX phase materials are also promising, but issues with sample preparation and batch-to-batch variability could delay the project.

- Additional work is required, in consultation with system vendors and component manufacturers, to determine acceptable reliability targets. Typically, life assessment for metallic materials is done with deterministic failure models and so we cannot directly map the statistical estimates of ceramic component lives to current life assessment approaches. Determining target reliability values would provide the missing piece of information needed to make fair design comparisons. Ideally, the target reliability of ceramic components would map to the expected or actual reliability of metallic components in service. However, given the limited amount of available in-service failure data a more theoretical approach may be required to link deterministic and statistical life assessment approaches.

2 Implementation and Verification of Time-independent Ceramic Failure Models

This chapter describes the implementation and verification of several models for the time-independent failure of advanced ceramic materials.

These models all start from the uniaxial failure statistics for a heat of ceramic material, for example as quantified by a series of four-point bend tests (see Chapter 3). The goal of these models is to extend that uniaxial failure model to arbitrary states of stress and account for the size effect. The size effect here is the fact that the larger the sample volume the more likely it will be to find a critical flaw in that volume. That is, for ceramics, larger equals weaker. Figure 2.1 is a taxonomy of the various models implemented in *srlife*.

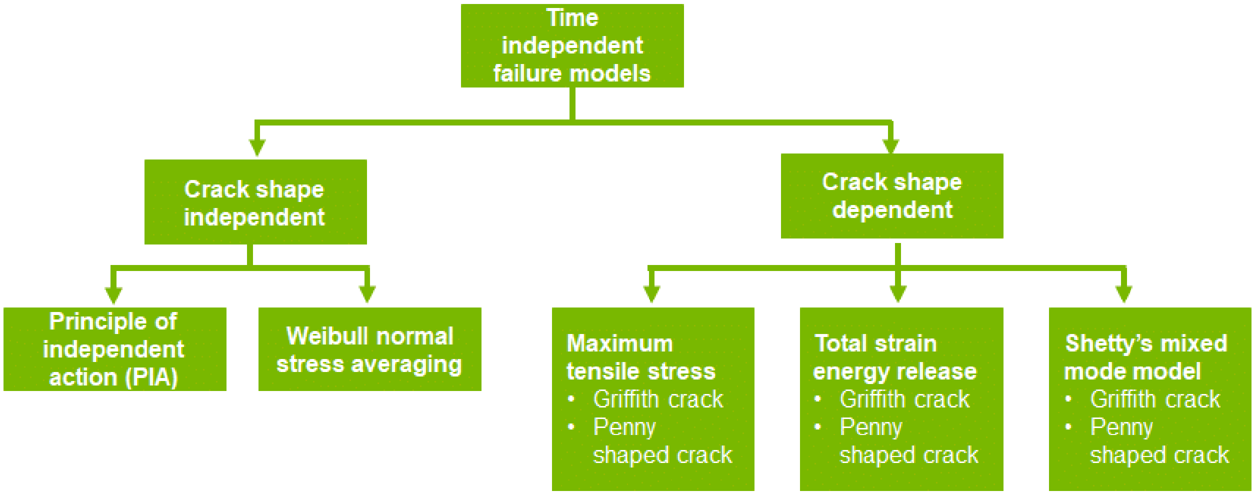
Time independent failure models
Crack shape independent
Crack shape dependent
Principle of independent action (PIA)
Weibull normal stress averaging
Maximum tensile stress
• Griffith crack
• Penny shaped crack
Total strain energy release
• Griffith crack
• Penny shaped crack
Shetty's mixed mode model
• Griffith crack
• Penny shaped crack

Figure 2.1. Flow chart of time independent failure models implemented in *srlife*..

The flow chart categorizes the models based on their dependency on the crack shape (geometry) and fracture criteria. The models have been developed to account for polyaxial stresses, under the assumption that all the flaws are volume based or distributed throughout the volume. The polyaxial stresses defined by the stress tensor is provided by the structural analyses in *srlife*. The material parameters (or characteristics) considered by assuming volume-based flaws are: Weibull modulus (m_v), characteristic strength ($\sigma_{\theta v}$), scale parameter (σ_{0v}), and uniaxial Batdrof crack density coefficient (k_{wv}), which are estimated from experimental test data

The following subsections describe each model in detail.

2.1 Principle of Independent Action (PIA)

This concept involves considering only the tensile principal stresses ($\sigma_{1,}\sigma_{2,}\sigma_3 \geq 0$) assuming they act independently and predicting the probability of failure (P_{fV}) using the Eq. (2.1) for a small, uniformly stressed volume element (ΔV) [8-9].

$$P_{fV} = 1 - exp\left(-k_{wV}\int_V ({\sigma_1}^{m_V} + {\sigma_2}^{m_V} + {\sigma_3}^{m_V})\,\mathrm{d}V\right) \tag{2.1}$$

or:

$$P_{f_V} = 1 - exp\left(-k_{w_V}\sum_i^n (\sigma_1^{m_V} + \sigma_3^{m_V} + \sigma_3^{m_V})\Delta V_i\right) \tag{2.2}$$

where; $\sigma_i = 0\ if\ \sigma_i \leq 0$.

Note: In the PIA model, compressive stresses are not assumed to contribute to the failure probability, and hence, their corresponding principal stresses are taken to be zero. Whereas, in the rest of the models, when a principal compressive stress exceeds the max principal tensile stress (for the same element) by a factor of three, the corresponding reliability is set to unity as per the CARES manual specification [7].

2.2 Weibull Normal Stress Averaging (WNSA)

This concept involves considering only the average normal tensile stresses $\overline{(\sigma_n)}$ in predicting the failure probability [10-11]. These stresses are evaluated as shown in Eq. (2.3), from the normal tensile stresses (σ_n) resolved on planes discretized over the surface of a sphere (of unit radius) defined in principal stress space $(\sigma_{1,}\sigma_{2,}\sigma_3)$. The failure probability in Eq. (2.4) involves using a polyaxial Batdrof crack density coefficient $(\overline{k_{wpv}})$, which is derived by equating the failure probability for uniaxial loading, to the failure probability for polyaxial loading, when the latter is reduced to a uniaxial condition (Eq. (2.5)).

$$\overline{\sigma_n}^{m_V} = \overline{\sigma_n}^{m_V} = \frac{\int_A {\sigma_n}^{m_V}\, dA}{\int_A dA} \tag{2.3}$$

$$P_{fV} = 1 - exp\left(-\int_V k_{wpV}\overline{\sigma_n}^{m_V}\, dV\right) \tag{2.4}$$

or

$$P_{f_V} = 1 - exp\left(-k_{wpv}\sum_i^n (\overline{\sigma_n}^{m_V})\Delta V_i\right) \tag{2.5}$$

$$k_{wpv} = (2m_V + 1)k_{wv} \tag{2.6}$$

2.3 Crack shape dependent models

The next category of models are crack shape dependent models. These were originally developed by Batdorf and Heinisch [12] and are based on mixed-mode fracture mechanics. These models combine (1) an assumed crack geometry with (2) a mixed-mode fracture criteria to completely describe the model. As such, any combination of a crack geometry in the next subsection and a mixed-mode failure criteria in the subsequent section can be combined.

2.3.1 Crack geometry

The incremental probability of failure under an applied stress Σ in a small, uniformly stressed volume element (ΔV) can be written as the following product:

$$\Delta P_{f_V}(\Sigma, \sigma_{cr}, \Delta V) = \Delta P_{1V} P_{2V} \tag{2.7}$$

where the product terms described by Batdorf and Crose [13] are:

$$\Delta P_{1V} = \Delta V \frac{dN_V(\sigma_{cr})}{d\sigma_{cr}} d\sigma_{cr} \tag{2.8}$$

ΔP_{1V} is the probability of the existence of a crack having a critical stress between σ_{cr} and $\sigma_{cr} + \Delta\sigma_{cr}$, in the volume ΔV, and

$$P_{2V} = \frac{\Omega(\Sigma, \sigma_{cr})}{4\pi} \tag{2.9}$$

is the probability of a crack of critical stress σ_{cr} oriented in a direction, such that the effective stress on it is greater i.e. $\sigma_e \geq \sigma_{cr}$. The critical stress σ_{cr} is the remote uniaxial strength of a given crack in Mode I loading, and the effective stress σ_e on the crack is based on the normal σ_n and shear τ components of the total traction vector σ acting on the crack plane.

The term $N_V(\sigma_{cr})$ is the Batdorf crack density function, and $\Omega(\Sigma, \sigma_{cr})$ is the area of a solid angle projected onto a unit radius sphere in principal stress space containing all crack orientations for which $\sigma_e \geq \sigma_{cr}$. The solid angle area depends on the (i) fracture criterion (ii) crack configuration, and (iii) applied stress. The angle is determined numerically in most cases using the following equation:

$$\Omega(\Sigma, \sigma_{cr}) = \int_0^{\frac{\pi}{2}} \left(\int_0^{\frac{\pi}{2}} \sin\alpha \, d\alpha \right) d\beta \, H(\sigma_e, \sigma_{cr}) \tag{2.10}$$

where $H(\sigma_e, \sigma_{cr}) = \begin{cases} 1 & ; \ \sigma_e \geq \sigma_{cr} \\ 0 & ; \ \sigma_e < \sigma_{cr} \end{cases}$

The integration limits are based on the symmetry of σ_e in the principal stress space, and hence, are defined for only the first octant of a unit sphere. Next, the component failure probability is calculated for applied stresses varying from 0 to $\sigma_{e_{max}}$: which is the maximum effective stress a randomly oriented flaw could experience. The failure probability is obtained by substituting Eq (2.8) and Eq. (2.9) in Eq (2.7) to get the following expression:

$$P_{f_V} = 1 - exp\left\{ -\int_V \left[\int_0^{\sigma_{e_{max}}} \frac{\Omega(\Sigma, \sigma_{cr})}{4\pi} \frac{dN_V(\sigma_{cr})}{d\sigma_{cr}} d\sigma_{cr} \right] dV \right\} \tag{2.11}$$

The integration limits signify that for any given crack, the σ_{cr} can vary from 0 to $\sigma_{e_{max}}$. On substituting Eq (2.10) into Eq (2.11), the σ_{cr} is replaced by σ_e as implied by the case for $H(\sigma_e, \sigma_{cr})$ where $\sigma_e \geq \sigma_{cr}$. This is done to cover the flaws on which the effective stress exceeds their critical stress. Therefore, their crack density functions will be written as:

$$N_V(\sigma_e) = k_{Bv}\,\sigma_e^{m_V}(x, y, z, \alpha, \beta) \tag{2.12}$$

Substituting the above crack density function (with the effective stress) and the solid angle in Eq (2.10), and integrating with respect to σ_{cr} we get the following form:

$$P_{f_V} = 1 - exp\left[-\frac{2}{\pi}\int_V \left[\int_0^{\frac{\pi}{2}}\int_0^{\frac{\pi}{2}} N_V(\sigma_e)\,sin\,\alpha\,d\alpha\,d\beta\right] dV\right] \tag{2.13}$$

To implement Eq (2.13) into a finite element method which involves discrete volume elements V_i, with Gaussian integration points at which the failure probability is evaluated, the equation can be used in the following numerical form:

$$P_{f_V} = 1 - exp\left\{-\frac{2k_{Bv}}{\pi}\sum_{i=1}^{n} V_i \left[\int_A \sigma_e^{m_v}(\alpha, \beta) dA\right]_i\right\} \tag{2.14}$$

To formulate crack shape dependent models, the effective stress σ_e is required to be evaluated. As mentioned earlier, the effective stress is evaluated using σ_n Eq (2.16) and τ Eq (2.17), and their expression depends on the crack orientation in principal stress space. Hence, we then define the total stress on the oriented crack through the principal stresses and direction cosines Eq.(2.15).

$$\sigma^2 = (\sigma_1 l)^2 + (\sigma_1 m)^2 + (\sigma_1 n)^2 \tag{2.15}$$

where $l = \cos\alpha, m = \sin\alpha\cos\beta, and\ n = \sin\alpha\sin\beta$; are the direction cosines for the traction vector σ as shown in the Fig. 2.2.

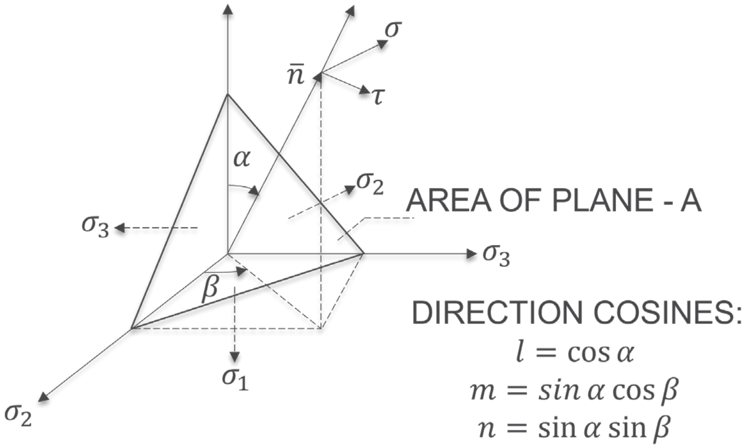

Figure 2.2. Direction cosines l, m and n of the stress tensor σ in principal stress space.

Based on the above figure, the normal stress on the crack plane is defined as:

$$\sigma_n = \sigma_1 l^2 + \sigma_2 m^2 + \sigma_3 n^2 \tag{2.16}$$

and the shear stress component as:

$$\tau^2 = \sigma^2 - \sigma_n^2 \tag{2.17}$$

2.3.2 *Mixed-mode failure criteria*

To evaluate the effective stress σ_e, the crack shape and fracture criteria must be specified. According to Batdorf and Heinisch [12] the assumption that fracture occurs when the local stress at some point on the surface of the crack cavity reaches the ultimate strength of the material, leads to the criteria that depend on crack shape. The criteria shown in the flow-chart (Fig. 2.1) are adopted from literature and implemented here.

2.3.2.1 Griffith's maximum tensile stress (MTS) criteria

In case of a Griffith crack, the solution for the effective stress is:

$$\sigma_e = \frac{1}{2}\left\{\sigma_n + \sqrt{\sigma_n^2 + \tau^2}\right\} \tag{2.18 8}$$

whereas the solution for a Penny shaped crack (which has greater shear sensitivity) is:

$$\sigma_e = \frac{1}{2}\left\{\sigma_n + \sqrt{\sigma_n^2 + \left(\frac{\tau}{1 - 0.5\upsilon}\right)^2}\right\} \tag{2.19}$$

where υ is the Poisson ratio.

2.3.2.2 Griffith's total co-planar strain energy release rate (CSE) criteria

The total strain energy release rate is expressed in terms of the different modes of loading as:

$$G_T = G_I + G_{II} + G_{III}$$

The above equation can be re-written in terms of the stress intensity factors (K) as:

$$K_{IC}^2 = K_I^2 + K_{II}^2 + \frac{K_{III}^2}{1 - \upsilon} \tag{2.20}$$

which becomes a criterion to help derive the solution for the effective stress. Here $K_I = \sigma_n\sqrt{\pi a}$ and $K_{II} = \tau\sqrt{\pi a}$ where 2a is the crack length. In case of a Griffith crack (assuming mode I and II dominate and III is neglected) the solution is:

$$\sigma_e = \sqrt{\sigma_n^2 + \tau^2} \tag{2.19}$$

and in case of a Penny shaped crack (which has greater shear sensitivity) the solution is:

$$\sigma_e = \sqrt{\sigma_n^2 + \left(\frac{\tau}{1 - 0.5\upsilon}\right)^2} \tag{2.20}$$

The above two criteria are formulated assuming the cracks grow/extend in their own plane, an assumption that can lead to a too high fracture stress [12].

2.3.2.3 Shetty's mixed-mode (SMM) criteria

Shetty in his work [14] implemented a modified equation proposed by Palaniswamy and Knauss [15], on the mixed-mode fracture of structural ceramics, based on the stress intensity factors. The equation's final form is:

$$\frac{K_I}{K_{IC}} + \left(\frac{K_\delta}{\bar{C}K_{IC}}\right)^2 = 1 \tag{2.21}$$

where K_δ can be either K_{II} or K_{III}, whichever is dominant and $\bar{C}$ is an empirical constant adjusted to best fit the data. Shetty found a range values of $0.8 \le \bar{C} \le 2.0$ for materials such as soda-lime glass and various ceramics with large cracks. The value of $\bar{C}$ is proportional to shear insensitivity in the above equation. Substituting the normal and shear stresses in Eq (2.23), the solution for the equivalent stress for a Griffith crack is:

$$\sigma_e = \frac{1}{2}\left[\sigma_n + \sqrt{\sigma_n^2 + \left(\frac{2\tau}{\bar{C}}\right)^2}\right] \tag{2.22}$$

and for a penny-shaped crack is:

$$\sigma_e = \frac{1}{2}\left[\sigma_n + \sqrt{\sigma_n^2 + \left(\frac{4\tau}{\bar{C}(2 - \nu)}\right)^2}\right] \tag{2.23}$$

2.3.3 Comparison

To compare all the above criteria, including WNTSA, a polar diagram plot can be made of the effective stresses as a function of crack orientation, which is basically a 2D projection of the 3D stress state. Assuming for simple tension case: $\sigma_n = \sigma\cos(\theta)^2$ and $\tau = \sigma\cos(\theta)\sin(\theta)$, the evaluated σ_e for an arbitrary criteria can be shown in Fig. 2.3(a) from Batdorf and Heinisch [12]. A polar plot is created from all the criteria (presented earlier) and shown in Fig. 2.3(b) The arrows indicate the direction of the conservativeness between the models.

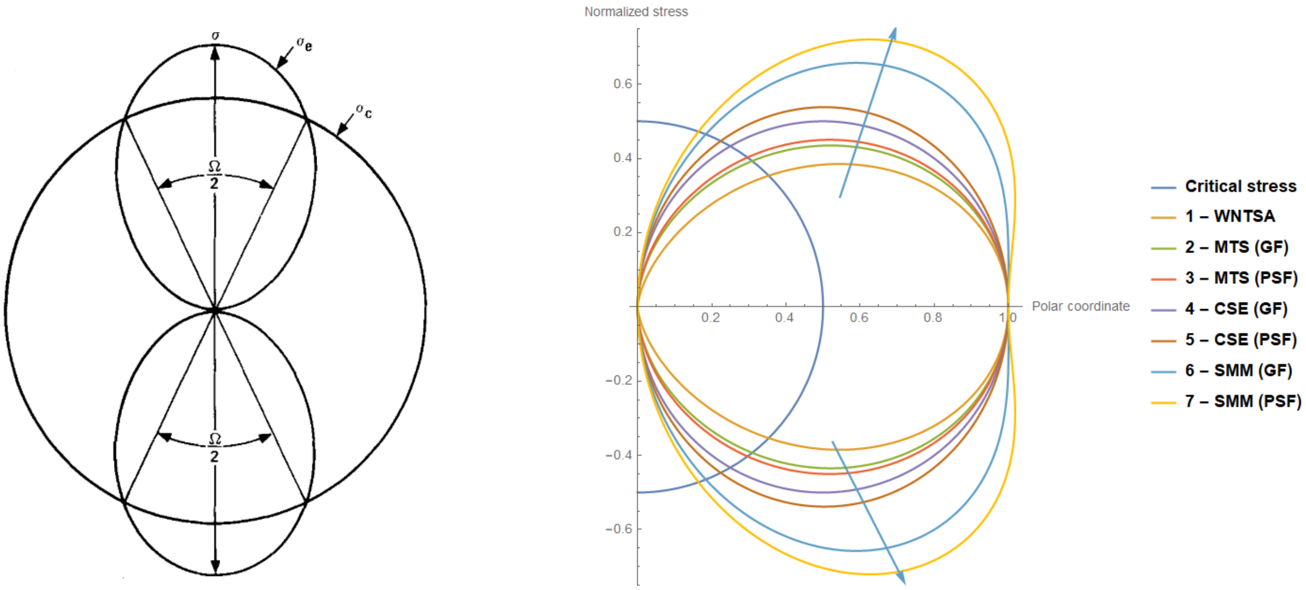

(a) (b)

Figure 2.3. (a) Polar plot of solid angle Ω containing all crack normals for which effective stress > critical stress. (b) Polar plot showing the effective stress/normal stress for all the models presented in Chapter 3, with respect to the critical stress. GF denotes Griffith crack/flaw and PSF denotes penny shaped crack/flaw.

2.4 Verification

The validation is done by simulating the test case presented in CARES manual [7] and comparing the results. In the test case a circular disk is transversely loaded, and its failure probability is calculated using all the models. The problem statement is as follows:

i. A circular disk made of Alumina is simply supported and transversely loaded as demonstrated experimentally in Rufin and Bollard [17] as shown in Fig. 2.4.
ii. The disk dimensions are: diameter = 51.6 mm, thickness = 1.8 mm
iii. The radius of support = 23.4 mm
iv. The radius of pressurized area = 23.4 mm
v. Material properties of Alumina are:
    i. Youngs modulus = 405 GPa
    ii. Poisson ratio = 0.25
vi. The parameters obtained after a Weibull fit to the experimental data are:
    ✓ $m_V = 28.53$
    ✓ $\sigma_0 = 169.7\ MPa\ m^{3/28.53}$ or $350.8\ MPa\ mm^{3/28.53}$
    ✓ $k_{wpv} = 58.06$
vii. The transverse disk loading was varied from 1.24 and 1.79MPa (180 to 260 psi) and the failure probability was evaluated at discretized values of pressure.

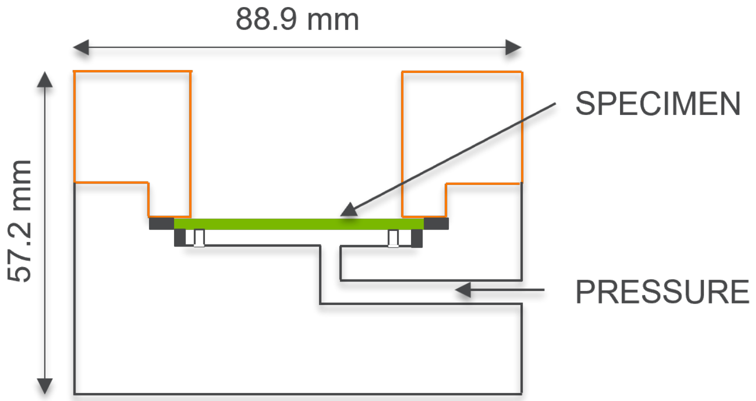
88.9 mm
57.2 mm
SPECIMEN
PRESSURE

Figure 2.4. Pressurized disk experimental test.

viii. In the CARES manual, a finite element (FE) method was implemented on a 7.5 degree segment of the disk. Based on the stresses obtained from the FE analysis, the failure probability was evaluated for the whole disc.

ix. For the *srlife* model validation, a FE method was implemented on a disk segment of 45 degrees as shown in Fig. 2.6 and the failure probability was obtained similarly for the whole disc.

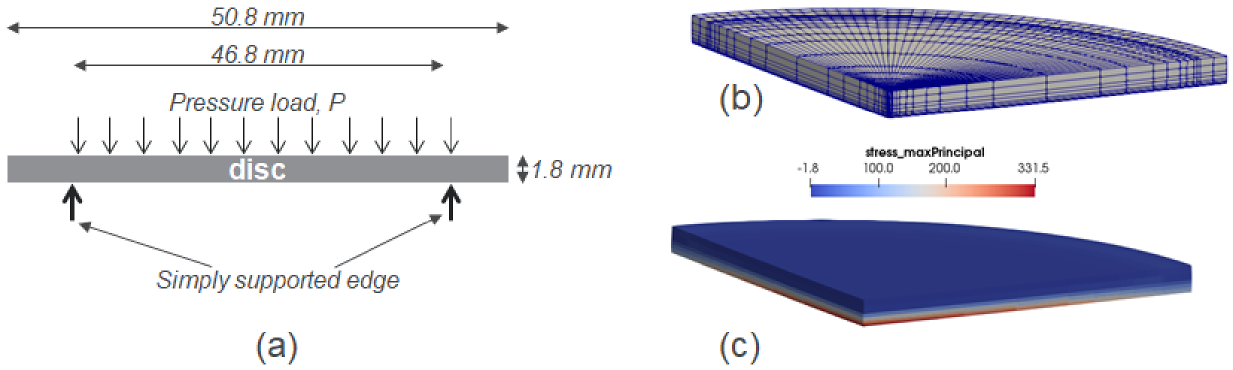
50.8 mm
46.8 mm
Pressure load, P
disc
1.8 mm
Simply supported edge
(a)
(b)
stress_maxPrincipal
-1.8
100.0
200.0
331.5
(c)

Figure 2.5. (a) Geometry, loading, and boundary condition (b) quarter symmetry 3D finite element model, and (c) example results from structural analysis of the transversely loaded circular disc example provided in CARES/LIFE manual [3].

x. A comparison between the results obtained from both the CARES and *srlife* model is shown in the Table 2.1, and the values are plotted in Fig. 2.7 As observed from the data and plots, the results from *srlife* match with those from CARES manual.

xi. A comparison between the experimental data from Rufin and Bollard [16] and the *srlife* curves in Fig. 2.8, shows the Shetty model for the penny shaped flaw is closest to the experimental data, similar to what was observed in the CARES manual.

On the basis of this comparison, we conclude that we correctly implemented all the time independent ceramic failure models.

Table 2.1. Comparison between probability of failure values obtained from PIA and WNTSA models for different mixed stresses.

Pressure	**Probability of failure (Pfv)**							
(MPa)	***srlife***							
	PIA	*Weibull*	*MTS*		*CSE*		*SMM*	
			GF	*PSF*	*GF*	*PSF*	*GF*	*PSF*
1.24100	0.00018	0.00080	0.00096	0.00101	0.00116	0.00135	0.00634	0.02303
1.31000	0.00082	0.00373	0.00449	0.00472	0.00543	0.00632	0.02936	0.10335
1.37900	0.00355	0.01605	0.01928	0.02024	0.02327	0.02705	0.12092	0.37616
1.44800	0.01424	0.06309	0.07538	0.07904	0.09044	0.10453	0.40485	0.85045
1.51700	0.05270	0.21800	0.25605	0.26710	0.30076	0.34076	0.85893	0.99923
1.58600	0.17520	0.58310	0.65084	0.66894	0.71993	0.77288	0.99906	1.00000
1.65500	0.47740	0.94760	0.97117	0.97590	0.98629	0.99323	1.00000	1.00000
1.72400	0.87530	0.99990	0.99999	0.99999	1.00000	1.00000	1.00000	1.00000
1.79300	0.99830	0.99990	1.00000	1.00000	1.00000	1.00000	1.00000	1.00000

Pressure	**Probability of failure (Pfv)**							
(MPa)	**CARES**							
	PIA	*Weibull*	*MTS*		*CSE*		*SMM*	
			GF	*PSF*	*GF*	*PSF*	*GF*	*PSF*
1.24100	0.00020	0.00080	0.00100	0.00100	0.00120	0.00140	0.00650	0.02400
1.31000	0.00090	0.00390	0.00450	0.00480	0.00500	0.00640	0.03010	0.10740
1.37900	0.00370	0.01670	0.01930	0.02070	0.02340	0.02730	0.12380	0.38810
1.44800	0.01490	0.06560	0.07550	0.08050	0.09100	0.10530	0.41230	0.86130
1.51700	0.05520	0.22580	0.25610	0.27130	0.30210	0.34270	0.86520	0.99940
1.58600	0.18260	0.59730	0.65070	0.67540	0.72160	0.77490	0.99920	1.00000
1.65500	0.49290	0.95330	0.97110	0.97740	0.98650	0.99340	1.00000	1.00000
1.72400	0.88650	0.99990	1.00000	1.00000	1.00000	1.00000	1.00000	1.00000
1.79300	0.99870	1.00000	1.00000	1.00000	1.00000	1.00000	1.00000	1.00000

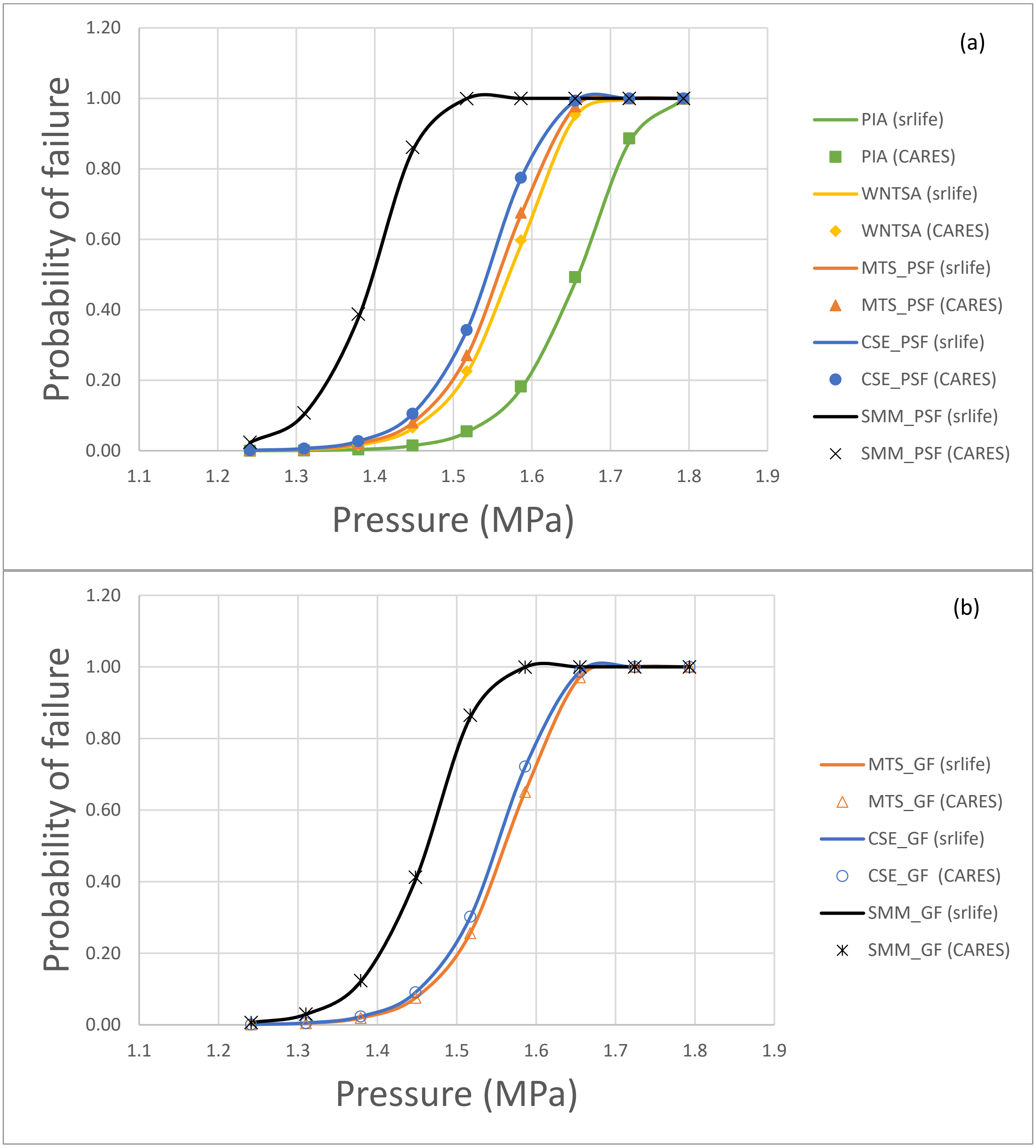

Figure 2.6. Comparison of failure probabilities from CARES manual (symbols) and srlife, generated using the models (a) PIA, WNTSA, MTS, CSE, and SMM for penny-shaped flaw and (b) MTS, CSE and SMM for Griffith flaw.

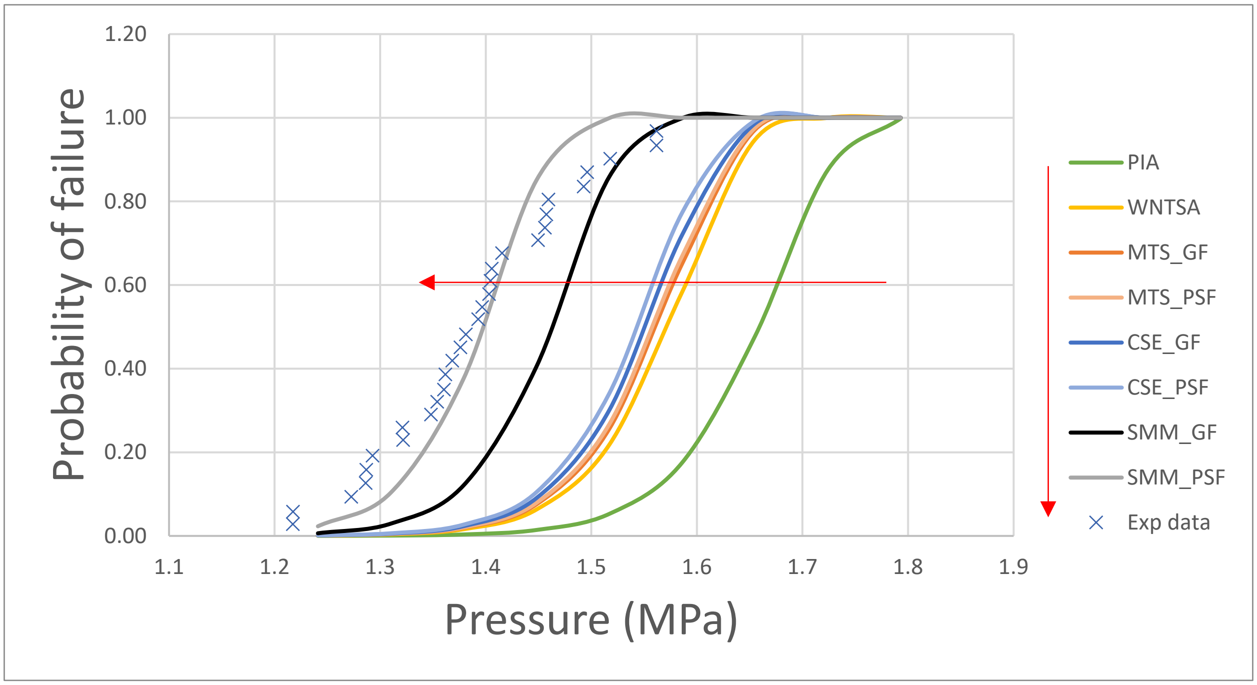

Figure 2.7. Comparison of failure probabilities predicted from all the models implemented in srlife, with the experimental data from Rufin and Bollard [16].

2.5 Summary and discussion

Figures 2.3 and 2.8 show that the order of *conservativeness* (shown the red arrow direction) between the models is as follows:

PIA < WNTSA < MTS_GF < MTS_PSF < CSE_GF < CSE_PSF < SMM_GF < SMM_PSF

A model is said to be more conservative in comparison to another model if it predicts a higher probability of failure for a given state of stress. Amongst all the fracture-based models, the Shetty model for a penny shaped flaw/crack is observed to be the most conservative, and closest to the experimental data.

However, the order of the conservativeness is slightly different for the reference receiver problem discussed below. For the reference receiver problem, CSE model turns out to be the most conservative, followed by SMM, MTS, WNTSA, and PIA. However, the CSE model may be too conservative because it is agnostic towards the type of stress. The equivalent stress in the CSE model is calculated on positive values of the normal and shear stresses, even if they are compressive in nature. Since the condition of setting reliability to unity is applied in the CARES manual and *srlife* tool, the effect of compressive stresses is falsely seen as tensile in the expressions of the CSE model. This results in lowering the reliability (of the CSE model) compared to other models. Hence, it is recommended to not use the CSE model, when applying *srlife* on ceramic receivers.

The remaining models are all at least reasonable for use in design evaluations. The Shetty models may be more accurate but require the Shetty coefficient, which in turn requires biaxial failure data to determine. If this data is available, we recommend the use of this model. If it is not available, we recommend the MTS model as a simple model that does not require multiaxial failure data.

3 High Temperature Ceramic Material Data

3.1 Overview

We conducted tests on a Si-C commercial grade ceramic to demonstrate the types of testing required to produce ceramic failure models of the type. To report its failure strength data, four-point flexure tests were conducted on rectangular beam shaped samples of the ceramic with dimensions as shown in the Table 3.1, and test configuration as shown in Figure 3.1. Tests were conducted at room temperature (RT) and high temperature (HT = 750° C) following ASTM standards C1161-18 [17] and C1211-18 [18], respectively. The room temperature tests were conducted in the Applied Materials Division at Argonne National Laboratory, while the high temperature tests were conducted at Touchstone Testing Lab.

Table 3.1. Average dimensions of samples

Average	
Width (mm)	4.05
Height (mm)	2.99
Length (mm)	45.71

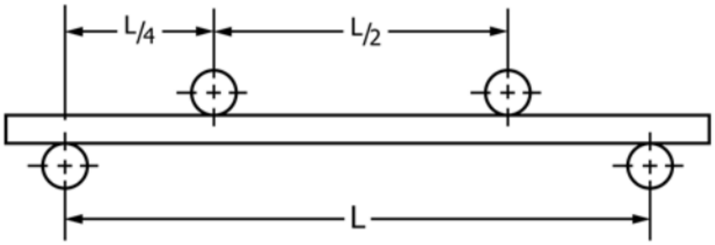

Figure 3.1. Configuration of four-point bend test where L = 40 mm.

3.2 Experimental results

The four-point flexure tests were conducted up to failure at each temperature, and the peak load was recorded. The load value was then used to determine the flexure strength using Eq. (3.1). The above steps were performed for all the tests conducted at RT and HT. A summary of the tests conducted, and results is shown in Table 3.2.

$$\sigma_f = \frac{3}{2}\frac{F * (L - l)}{bh^2} \tag{3.1}$$

where the length L represents supports span and l represents the load span.

Table 3.2. Summary of tests conducted, and results obtained.

Material	Experimental data			
SiC	Temperature (°C)	Number of tests performed	Unbiasing factor	Flexure strength (MPa)
Commercial grade	28	14	0.901	252.074
	750	15	0.908	250.229

To understand the evolution of the flexural strength with temperature the strengths are plotted in Figure 3.2 to show a comparison between the data obtained at the respective testing temperatures. The data shows that the average strength remains unchanged, as it decreases only by 2 MPa (from 252 MPa to 250 MPa) when the temperature increases from 28° C to 750° C. A comparison of the current experimental values with those from literature for a dense sintered commercial α- SiC is shown in Figure 3.3. The values from literature are overall larger than those obtained from current experiments, but they too remain unchanged with temperature, as they show only a drop in average strength of 2 MPa, from 20° C to 800° C.

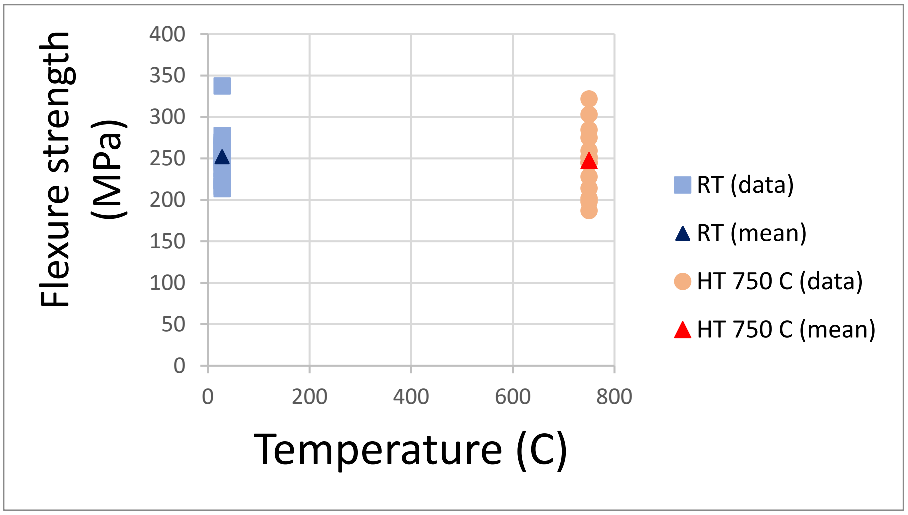

Figure 3.2. Flexure strength (MPa) vs density (g/cc) from high temperature tests on SiC commercial grade.

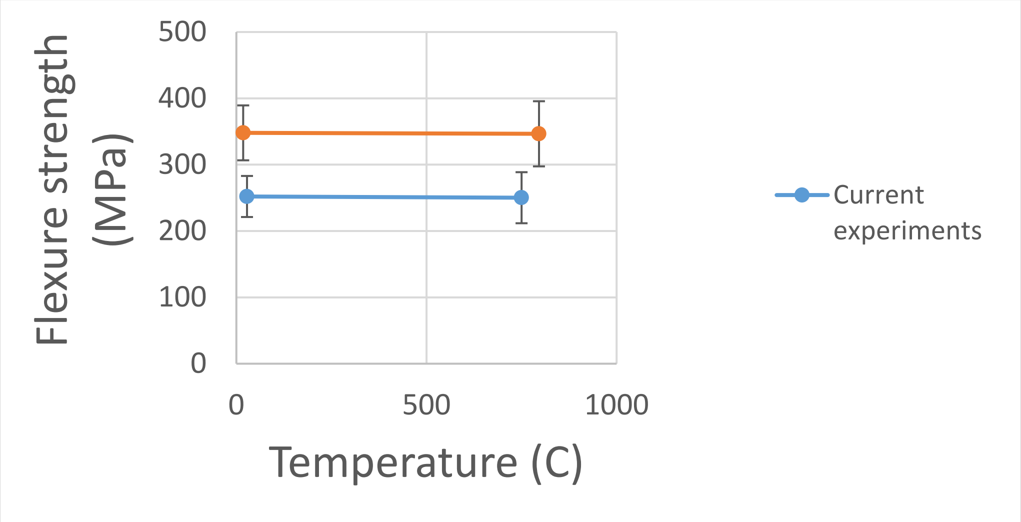

Figure 3.3. Comparison of flexure strength (MPa) data from current experiments on commercial SiC and literature values on α- SiC [21].

3.3 Processing the data

In this section the flexure strength data and the dimensions of the samples are used to estimate the Weibull distribution, following ASTM standard C1239-13 [19]. In the ASTM standard, the probability that an advanced ceramic will fail under an applied uniaxial tensile stress σ is given by the cumulative distribution function Eq. (3.2) as formulated by Weibull [20].

Assuming the strength-controlling flaws are randomly distributed through the volume of the material, the distribution for volume-based flaws can be alternatively described by Eq. (3.3). The parameters in Eq. (3.2) are Weibull modulus (m), characteristic strength (σ_θ) (associated with test specimen), and they are estimated using flexure strength data from experiments [21]. A Weibull two parameter model (scripted in python) is used to fit the experimental data. The scale parameter (σ_0) (strength relative to unit size) is further evaluated using Eq. (3.5) where $m_V = m$, and eventually implemented in Eq. (3.3) to evaluate the failure probability. While the uniaxial Batdrof crack density coefficient (k_{wV}) is evaluated from the scale parameter in Eq. (3.6).

$$P_{fV} = \begin{cases} 1 - exp\left[-\left(\frac{\sigma}{\sigma_\theta}\right)^m\right] & if \quad \sigma > 0 \\ 0 \quad if \quad \sigma \leq 0 \end{cases} \tag{3.2}$$

$$P_{fV} = \begin{cases} 1 - exp\left(-\int_V \left(\frac{\sigma}{\sigma_{0v}}\right)^{m_V} \mathrm{d}V\right) & if \quad \sigma > 0 \\ 0 \quad if \quad \sigma \leq 0 \end{cases} \tag{3.3}$$

$$P_{fV} = 1 - exp\left(-k_{wV}\int_{V}\sigma^{m_V}\,\mathrm{d}V\right) \tag{3.4}$$

$$\sigma_{0v} = \sigma_{\theta}\left(\frac{V * \left(\left(\frac{L}{l}\right) * m_v + 1\right)}{2 * (m_v + 1)^2}\right)^{\frac{1}{m_v}} \tag{3.5}$$

$$k_{wv} = (\sigma_{0v})^{-m_v} \tag{3.6}$$

where $V = b * d * L$ is the volume of the gage section

Table 3.3. Weibull distribution parameter estimates for SiC (commercial grade). summarizes all the parameters obtained from fitting a Weibull two-parameter model to the flexure strength data from SiC. Figure 3.4 shows the calibrated probability distributions, and the legend in each plot shows the values of the fitted parameters. The plot axes are scaled in such a way that the fitted distribution (model) is a straight line. The experimental data points either fall on it or close to it and lie within the blue shaded region which represents the confidence intervals. The more the number of data points, the thinner is the confidence interval. The parameters σ_{θ} and m are determined using a maximum-likelihood function applied on the data, and the straight line is plotted using the parameters. The current parameter values were generated by assuming a unimodal failure distribution, with no censoring, similar to the method demonstrated in ASTM C1239 [18].

The scale parameter and the strengths are then used to evaluate the cumulative failure probability using Eq. (3.3) which is plotted for the SiC ceramic in Figure 3.5. The parameters m_v and σ_θ in Table 3.3 are observed to reduce with temperature, while σ_0 increases with temperature. As observed in Figure 3.5(a) the failure probability when evaluated using σ_θ increases with temperature, whereas in Figure 3.5(b) the failure probability evaluated using σ_0 decreases with temperature.

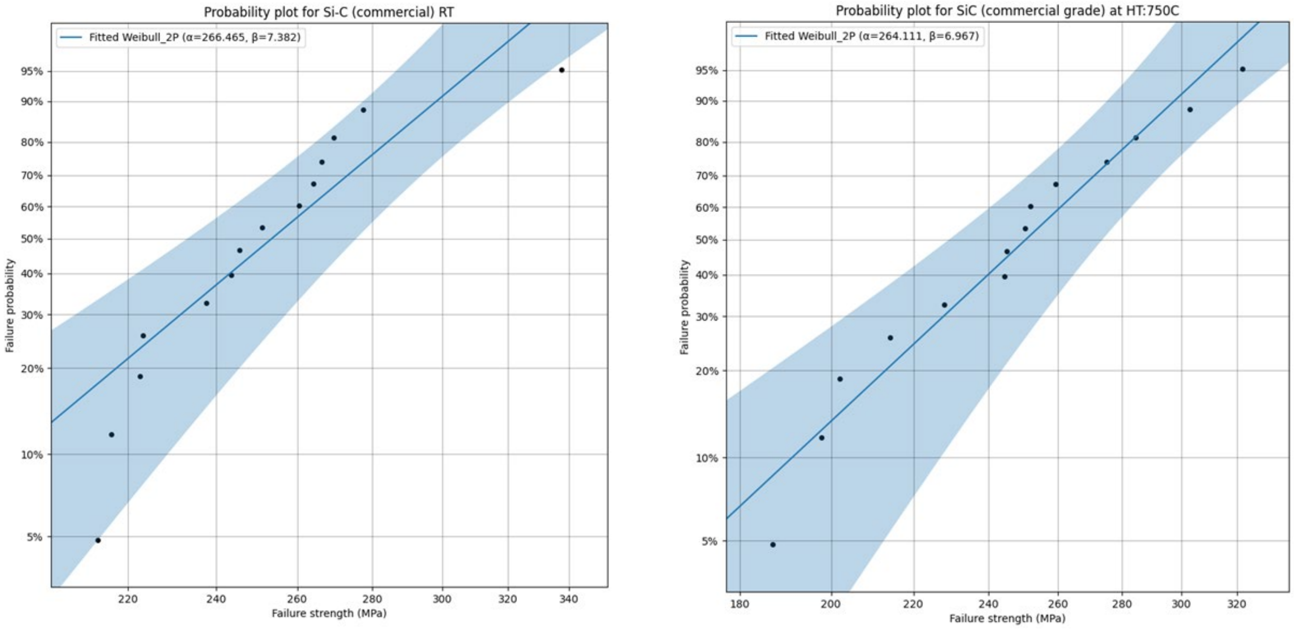

(a) (b)

Figure 3.4. Failure probability plots for SiC (commercial grade) at (a) room temperature (b) high temperature (750° C).

Table 3.3. Weibull distribution parameter estimates for SiC (commercial grade).

SiC	Weibull distribution parameters					
Commercial grade	Temperature (°C)	Weibull modulus (m_v)	Weibull modulus (m_v) *(unbiased)*	Characteristic strength (σ_θ) (MPa)	Scale parameter (σ_{0v}) (MPa-(mm)^(3/m))	Batdorf crack density coefficient **($\overline{k_{bv}}$)**
	28	7.38	6.65	266.46	411.28	14.3
	750	6.97	6.33	264.11	419.68	13.66

3.4 MAX phase test data

As a part of another on-going project, four-point flexure tests were conducted on Ti_3SiC_2 MAX Phase ceramic, at room temperature and several higher temperatures. A summary of the tests and results is provided in Table 3.4. The strength of the ceramic is plotted in Figure 3.6 and compared with respect data from literature. The MAX Phase ceramic is known to show a "brittle to plastic transition" around 1100° C, which is observed as a rapid drop in strength with temperature. The drop in strength from the current experiments was observed to be from 900° to 1000° C. It was then followed by a rise until 1200° C, which is an unusual trend compared to the those observed in the literature.

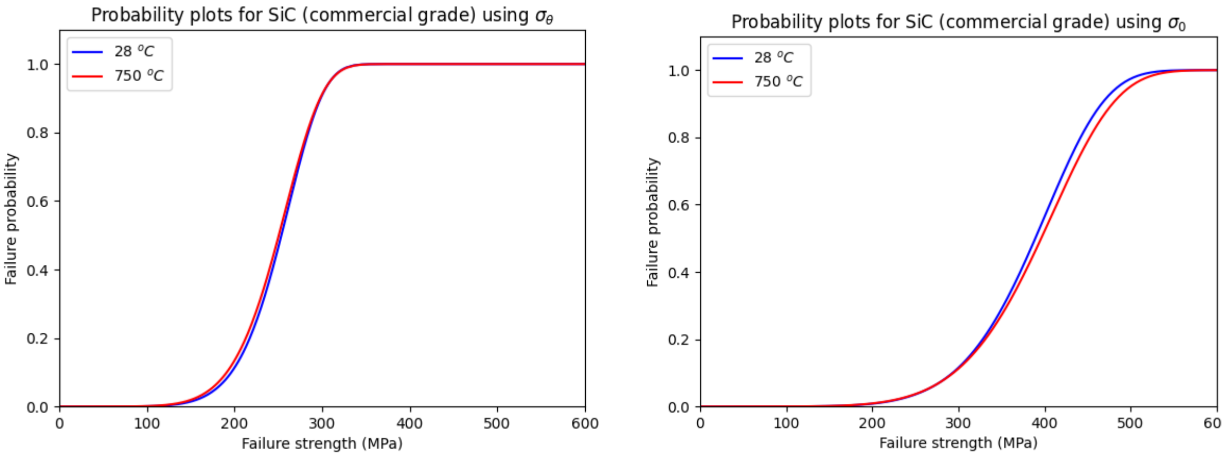

Figure 3.5. Cumulative probability distribution plots for SiC (commercial) using (left) characteristic strength σ_θ and (right) scale parameter σ_0 i.e. for unit volume.

Table 3.4. Summary of tests conducted on MAX Phase material.

Material	Experimental data		
	Temperature (°C)	Number of tests performed	Flexure strength (MPa)
Ti_3SiC_2	28	15	519.233
	800	2	464.5
	900	2	459.0
	1000	6	322.667
	1200	6	357.50

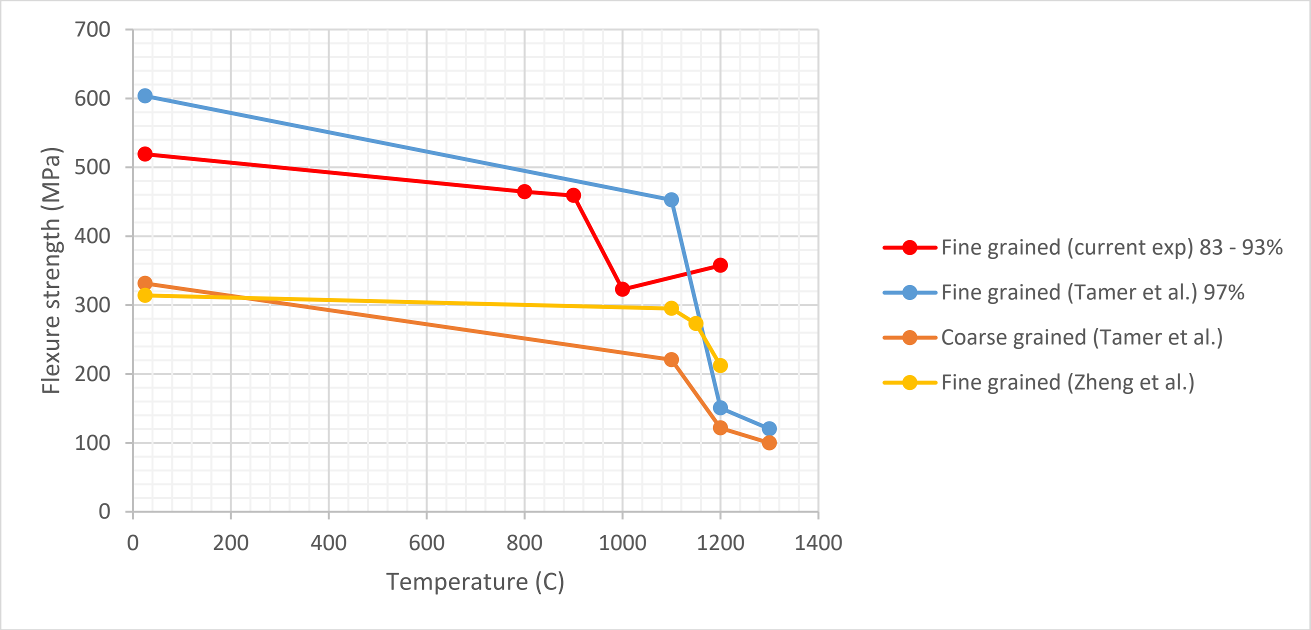

Figure 3.6. Plot of flexure strength (MPa) data from current experiments and literature values from MAX Phase of different phase contents (%) and grain structure.

4 Thermohydraulic Solver for Tubular Panel Receivers

srlife now includes a basic thermohydraulic model for calculating heat transfer from the net incident flux on a tubular panel receiver, through the tube material, and into the flowing working fluid. This new feature was not in the original proposed research plan. However, in the course of preparing models to compare ceramic receiver to metallic receiver designs we realized that integrating the thermohydraulic analysis into *srlife* greatly simplified the analysis required to make a fair comparison between comparable receivers made from widely different material categories.

Previously, a *srlife* user would need to complete the thermohydraulic analysis in a separate simulation code. The input to *srlife* proper was the net incident flux distribution on each tube in the receiver and the fluid temperature and flow rate along each tube in each flow path, as a function of the axial position along each tube. This information was sufficient to solve for the tube temperatures using a transient, 3D, finite different solver built into *srlife*.

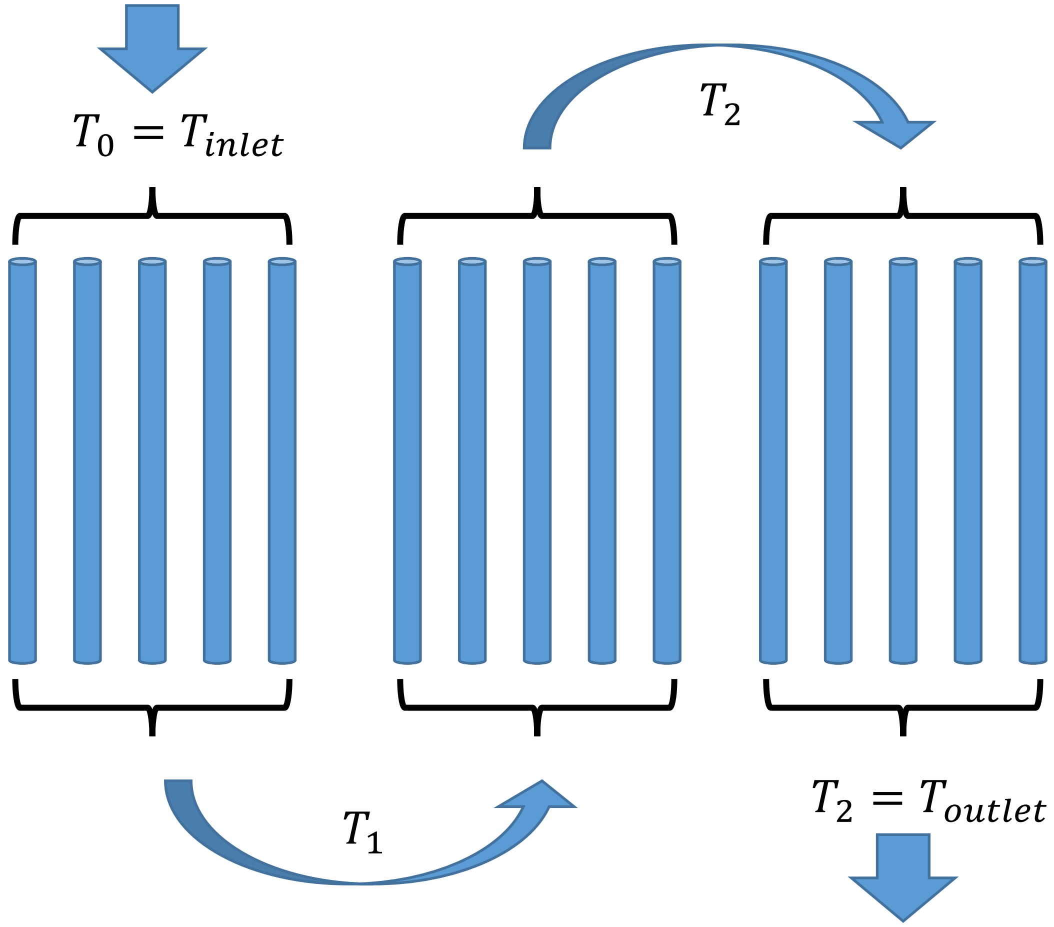

Figure 4.1. Simplified panel flow path model used in the thermohydraulic solver.

The thermal properties of ceramics and metals are significantly different. A fair comparison between a receiver with similar operating characteristics but constructed from two different materials would fix the incident flux (or at least the peak flux) and the fluid inlet and outlet temperatures. To meet these fixed conditions, either the tube thickness or the fluid flow rate will need to be varied from material to material. This will generally require iterating on, for example, the fluid flow rate in order to match the target outlet temperature. This iteration requires many individual thermohydraulic analyses to find the correct flow rates.

Iterating between *srlife* and an external thermohydraulic solvers is inconvenient and adds significantly to the time required to complete one analysis. Given that one of the objectives for *srlife* was to provide a fast tool for receiver life assessment [6] we decided to integrate the thermohydraulic analysis into *srlife* proper. This allows the user to execute an analysis of this type (i.e., find the required flow rate and then estimate the system life) in one step, without relying on external software.

We implemented a simple thermohydraulic solver in *srlife*. Figure 4.1 illustrates the basic data structure used in the analysis. We assign each panel in the receiver to an ordered flow path. Fluid starts at a user-specified (time-dependent) inlet temperature and mass flow rate and moves through each panel in in the flow path order. In each panel the fluid absorbs heat from the incident solar flux and carries part of that heat out of the panel through convection. The thermohydraulic solver then solves for the fluid temperature and flow rate along each point in the flow path, including the final outlet temperature and flow rate. In the process, it also solves for the coupled temperature field in the solid tubes.

The solver makes several simplifying assumptions to produce an efficient (fast) thermohydraulic solver that nevertheless captures the key details of heat transfer in a tubular panel receiver:

1. Frictional losses are negligible in solving for the flow rate. This means we can completely eliminate the fluid flow equations from the simulation and simply assume that the mass flow rate into and out of each panel in the flow path is constant.
2. The fluid temperature variation across each individual panel is linear. This means we do not have to solve a field equation along the flow path. Instead, we simply balance the heat entering and leaving each individual panel.
3. Each panel starts and ends in a manifold which perfectly mixes the fluid temperature. That is, the fluid temperature in each tube in a panel is the same at the start and end of the tube (though the start and end temperatures will be different).

The resulting solver is essentially a bookkeeping exercise. The unknown variables are the fluid temperatures in between each panel along a flow path (where the start temperature of panel $i+1$ is equal to the end temperature of panel i). The user provides the inlet temperature (i.e., the start temperature for the first panel) and the inlet flow rate. The solver then balances heat transfer within each panel to solve sequentially for the fluid temperature in between each panel in the flow path and at the final flow path outlet.

While each tube within a panel is generally identical, the incident solar flux on each tube in a panel is generally not the same. Therefore, the solver needs to be able to represent each individual tube in a panel. As an abstraction, we allow the user to provide the fluxes (and geometrical information) for a limited number of representative tubes in each panel along with a weight factor. This weight factor represents the number of actual tubes represented by each representative tube. For example, if there are 100 tubes in the actual panel and the user explicitly represents the panel with 3 representative tubes then valid panel weights might be 25, 50, and 25. The requirement is that the tube weights total to the actual number of tubes in the panel.

The thermohydraulic solver unknowns are the fluid temperatures in between each panel T_i where T_0 is the user-defined inlet temperature. The goal is to find each of these temperatures, for each flow path, as a function of time for a discrete number of time steps spanning the user-provided incident flux distributions. The following solution procedure solves these temperatures for a given, fixed time. The process can be repeated to solve for the transient temperature distribution.

4.1 Thermohydraulic solver procedure

The solver begins with a guess for each interpanel temperature T_i. By default, this guess is equal the converged temperature values for the previous time step. The user must provide the initial conditions for the entire flow path, in addition to the time-varying inlet temperature. The solver labels each panel with a pair of indices, i.e. panel 12 connects fluid temperatuers T_1 and T_2. The temperature distribution along each tube in a panel is then given by

$$T_{ij,k} = \frac{T_j - T_i}{l_{ij}}\left(z - l_{ij}\right) + T_i \tag{4.1}$$

with l_{ij} the tube height and z an arbitrary position along the tube. The fluid velocity in each tube is

$$v_{ij,k} = \frac{\dot{m}}{\rho(T) A_{ij,k}} \tag{4.2}$$

with $\dot{m}$ the flow path mass flow rate, $A_{ij,k}$ the tube cross-sectional area, and $\rho(T)$ our first material property correlation: the fluid density as a function of temperature. To further simply the analysis, we evaluate the fluid properties required in the analysis at the average tube temperature:

$$\bar{T}_{ij,k} = \frac{T_j + T_i}{2} \tag{4.3}$$

The fluid property dependence on temperature is omitted in the subsequent discussion, assumed always to be evaluated at the tube mean temperature.

The solver assembles a system of nonlinear equations representing heat balance in each panel in the flow path. Each panel provides a single equation, meaning a flow path with n panels has n equations. There are $n+1$ values describing the interpanel fluid temperatures. However, the first temperature in the chain (the inlet temperature) is fixed by the user, meaning the number of unknowns balances the number of heat balance equations.

For each individual panel the heat balance can be simply expressed as

$$\dot{Q}_{ij,mass} = \dot{Q}_{ij,conv} \tag{4.4}$$

that is, the heat transferred out of the panel by mass flow is balanced by the heat transferred into the panel by convection between the tube (in turn heated by the incident flux) and the moving fluid. We can simply describe each side of this heat balance equation with:

$$\dot{Q}_{ij,mass} = \dot{m}c_p\left(T_j - T_i\right) \tag{4.5}$$

where c_p is the temperature-dependent heat capacity of the fluid, evaluated again at the tube mean temperature, and

$$\dot{Q}_{ij,conv} = \sum_{k=1}^{n_{tube}} n_{ij,k} \int_0^{L_{ij,k}} \int_0^{2\pi} h\left(\bar{T}_{ij,k}, v_{ij,k}\right)\left(T_{metal}\,(\theta, z) - \frac{T_j - T_i}{l_{ij}}\left(z - l_{ij}\right) - T_i\right) r_{ij,k}\, d\theta dz \tag{4.6}$$

where n_{tube} is the number of representative tubes included in the user input, $h\left(\bar{T}_{ij,k}, v_{ij,k}\right)$ is the fluid convective heat transfer coefficient as a function now of both the mean tube fluid temperature and the fluid velocity, $T_{metal}\,(\theta, z)$ is the tube temperature on the inner diameter of the tube as a function of axial and circumferential position, and $r_{ij,k}$ is the tube inner radius.

Conceptually then, the thermohydraulic solver simply assembles the heat balance equations and solves them for each time step. However, there are two complications:

1. The fluid properties (density ρ, heat capacity c_p, and film coefficient h) all depend on temperature, meaning the resulting heat balance equations are nonlinear.
2. The amount of heat actually transferred into the fluid by convection between the inner tube wall and the fluid depends on the details of transient heat transfer between the net incident flux on each tube (which the user provides) and the convection on the tube inner diameter. That is, we need to solve a coupled, 3D heat transfer equation for the tube temperatures in order to specify the input heat in each panel.

We solved these challenges by:

1. Solving the nonlinear heat balance equations using Newton's method. This requires the Jacobian of the nonlinear system (i.e., the derivative of the discrete heat balance equations with respect to temperature). We obtained this Jacobian using automatic differentiation using the jax python module [23].
2. Using the existing 3D, finite different heat transfer solver built into srlife to solve for heat transfer between the incident flux and the fluid (i.e. through the solid tube) [6]. Previous work describes the verification and validation of this solver, which takes as input the incident flux into the tube and the convective heat transfer out of the tube into the working fluid.

#2 here poses yet another challenge, as the solid tube heat transfer solver is itself nonlinear with respect to the fluid temperature. We therefore use a nested set of iterative loops to solve for the temperatures in both the solid tubes and the fluid:

[Outer loop] Iterate between solid heat transfer and thermohydraulic solvers, using the film temperature as the interface between the two solvers.

[Inner loop #1] Solve for the fluid temperature using the process outlined above

[Inner loop #2] Solve for the tube solid temperatures using the existing 3D finite difference solver.

Both inner loops are solved using Newton's method. The outer iteration is solved using Picard iteration. This means convergence between the solid and fluid temperatures is less than optimal. If needed, we could improve convergence here by converting to Newton's method in the future.

4.2 Validating the thermohydraulic solver

Previous work describes the validation of the finite difference solid heat transfer solver, leaving only to validate the thermohydraulic heat transfer solver itself. We verified the model by comparing the numerical solution to two simple problems with analytical solutions: an isothermal case and a constructed case with constant fluid properties. In both cases a hand calculation can establish the temperatures along the flow path at all points.

We then validated the model by comparison to previous simulations where we used external software to calculate the fluid temperature along each flowpath in the receiver. Specifically, in the past we have assumed a linear temperature distribution along the entire flowpath. We validated the new thermohydraulic simulations by comparison to these past results. The fluid temperature profiles are different, specifically the new thermohydraulic receiver results in a somewhat nonlinear fluid temperature distribution. However, the overall results, including the final life estimation, match with the past results, suggesting that the new solver is providing accurate fluid temperature fields.

4.3 Fluid thermal properties

The new thermohydraulic solver requires detailed fluid properties for the receiver working fluid. Specifically, the model requires correlations for the fluid:

1. Density
2. Heat capacity

3. Convective film coefficient

As functions of the fluid temperature and flow velocity.

4.3.1 General material model

The general material model constructed for the solver assumes that the fluid density ρ, the heat capacity c_p, the dynamic viscosity μ, and the conductivity k are all polynomial functions of absolute temperature. The remaining material property is then the film coefficient, which we calculate using the Gneilinski [24] correlation:

$$Nu = \begin{cases} \dfrac{(f/8)(Re - 1000)Pr}{1 + 12.7\sqrt{f/8}(Pr^{2/3} - 1)} & Re \geq 2000 \\ 4.01 & Re < 2000 \end{cases} \tag{4.7}$$

with the friction factor given as

$$f = (0.79 \log Re - 1.64)^{-2} \tag{4.8}$$

and Re the Reynold's number and Pr the Prandtl number. We calculate the Reynold's number based on tubular flow:

$$Re = \frac{\rho v^2 r}{\mu} \tag{4.9}$$

The threshold in the Gneilinski correlation approximately accounts for laminar flow for very low flow velocities.

4.3.2 Specific fluid data

As discussed above, the thermohydraulic analysis in *srlife* requires temperature dependent properties of the heat transfer fluid flowing inside the receiver tubes. Table 4.1 lists the required fluid properties as polynomial functions of absolute temperature for a chloride salt. Tables 4.2 and 4.3 list the polynomial equations to calculate properties of supercritical carbon dioxide (sCO$_2$).

Table 4.1. Properties of chloride salt (32% MgCl2 / 68% KCl). Valid for temperature between 723K to 1073K.

Properties	*unit*	*Values as function of temperature, T (K)*
C_p [25]	W-hr/kg-K	$\frac{989.6+0.1046\times(T-273.15-430)}{3600}$
ρ [25]	kg/mm^3	$\frac{1903.7-0.552\times(T-273.15)}{10^9}$
μ [25]	kg/(mm-hr)	$\frac{(1.4965\times10^{-2}-2.91\times10^{-5}\times(T-273.15)+1.784\times10^{-8}\times(T-273.15)^2)*3600}{1000}$
K [25]	W/(mm-K)	$\frac{0.5047-0.0001\times(T-273.15)}{10^3}$

Table 4.2. Isobaric properties of sCO$_2$. Valid for temperature between 600K to 1050K.

Properties	*Unit*	*Values as function of temperature, T (K), coefficients are in Table 4.3*
C_p [26, 27]	W-hr/kg-K	$(a_3T^3 + a_2T^2 + a_1T + a_o) * (\frac{1000}{3600})$
ρ [26, 27]	kg/mm^3	$\frac{b_3T^3+b_2T^2+b_1T+b_o}{10^9}$
μ [26, 27]	kg/(mm-hr)	$(c_3T^3 + c_2T^2 + c_1T + c_o) * (\frac{3600}{1000})$
K [26, 27]	W/(mm-K)	$(d_1T + d_o) * (\frac{1}{1000})$

Table 4.3. Values of the coefficients in Table 4.2.

		Pressure				
		15 MPa	17.5 MPa	20 MPa	22.5 MPa	25 MPa
C_p	a_3	-9.4933233E-10	-1.1685899E-09	-1.3681834E-09	-1.5548926E-09	-1.7276167E-09
	a_2	2.5033584E-06	3.1301961E-06	3.7044140E-06	4.2423677E-06	4.7397405E-06
	a_1	-1.9712267E-03	-2.5808187E-03	-3.1434114E-03	-3.6712605E-03	-4.1595349E-03
	a_o	1.6815588E+00	1.8881690E+00	2.0805359E+00	2.2614582E+00	2.4292163E+00
ρ	b_3	-3.3073597E-07	-4.0624749E-07	-4.8330438E-07	5.6114332E-07	-6.3649998E-07
	b_2	1.0188972E-03	1.2453441E-03	1.4759544E-03	1.7084570E-03	1.9341521E-03
	b_1	-1.1274061E+00	-1.3673222E+00	-1.6107768E+00	-1.8554983E+00	-2.0937634E+00
	b_o	5.1621766E+02	6.1751149E+02	7.1956920E+02	8.2162318E+02	9.2138362E+02
μ	c_3	-2.0609813E-15	-5.3841198E-15	-9.4112643E-15	-1.4034587E-14	-1.9298371E-14
	c_2	-5.3958426E-14	9.7343653E-12	2.1501577E-11	3.4982102E-11	5.0257231E-11
	c_1	3.4009896E-08	2.3989810E-08	1.2087897E-08	-1.4827705E-09	-1.6761751E-08
	c_o	1.0295015E-05	1.4047191E-05	1.8416027E-05	2.3346716E-05	2.8842485E-05
K	d_1	6.8949965E-05	6.7610877E-05	6.6123439E-05	6.4498526E-05	6.2752351E-05
	d_o	4.6932789E-03	6.3413421E-03	8.1250053E-03	1.0040558E-02	1.2078258E-02

5 Assessing the Viability of Ceramic Receivers

We assessed the viability of ceramics as structural material for high temperature CSP receivers using a reference receiver model. The goal of the reference model is not to actually design a receiver, but rather to serve as a realistic test bed to assess different potential ceramic materials, such as SiC and Ti_3SiC_2 MAX Phase, for receiver tubes. The reference model is also used to assess different time-independent failure models of ceramics, as discussed above, in terms of their applicability and conservatism for designing high temperature ceramic receivers. Finally, a comparison between metallic and ceramic receiver designs is made using the reference receiver model.

5.1 Reference receiver

The reference receiver model is a 17 m diameter, 21 m tall, 360° external cylindrical receiver. Figure 5.1 shows the radiation heat flux map on the receiver at noon and the variation in heat flux during the day. We used SolarPILOT [28] to determine the heat flux map on the receiver through an optimization analysis for a thermal design power of 500 MW$_t$ and maximum DNI of 750 kW/m^2. Figure 5.1(a) indicates the heat flux map is symmetric about the north-south axis, we therefore considered two serpentine flow paths, each containing six panels for the heat transfer fluid (HTF). The HTF enters the receiver at the north side through Panel-1 and leaves the receiver at the south side through Panel-6. Each panel consists of 100 tubes with 42.2 mm outer diameter. We considered chloride salt (properties are in Table 4.1) as the HTF for the receiver. The HTF inlet and outlet temperatures are 550°C and 720°C, respectively.

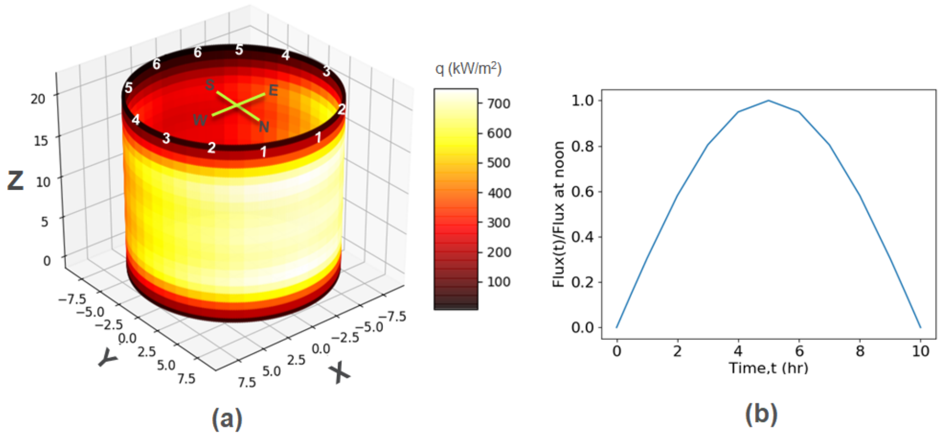

Figure 5.1. (a) Heat flux map on the reference receiver at noon. Numbers 1 to 6 indicates the panels in the receiver along two flow paths. (b) Heat flux variation during the day.

5.2 Thermohydraulic analysis

We performed thermohydraulic analysis of the reference receiver considering two representative tubes – one with the highest heat flux and one with the lowest heat flux – from each panel and considering a panel weight factor of 50 for each tube. A receiver may operate under constant design mass flow rate, variable mass flow rates to keep the HTF outlet temperature constant, or a combination of constant and variable mass flow rates. We considered variable mass flow rates for the reference receiver. The mass flow rate at each time step was optimized in an iterative manner so that the fluid outlet temperature is always about 720°C. Figure 5.2 plots the optimum mass flow rate for the reference receiver considering 1 mm thick tubes and SiC as the tube material. The figure also plots the HTF and tube crown temperatures along the flow path under the optimum mass flow rates. The figure plots these temperatures for the two representative tubes per panel considered in analysis. As the figure indicates, at the start of the day the fluid temperature is constant, 550°C along the flow path. As the incident heat flux is transferred to the HTF, the temperature changes to a nonlinear profile along the flow path, going from 550°C at the inlet to 720°C at the outlet. This fluid temperature profile stays nearly constant all day due to the variable mass flow rates. The tube crown temperature profile along the flow path, on the other hand, always changes with time following the changes in the incident heat flux and the convective film coefficient of the HTF. Figure 5.2 also shows a contour plot of tube outer surface temperature at noon for one of the two representative tubes per panel considered in analysis. The contour plot indicates large variation in tube temperature both along the axial and circumferential directions, as expected for an external receiver.

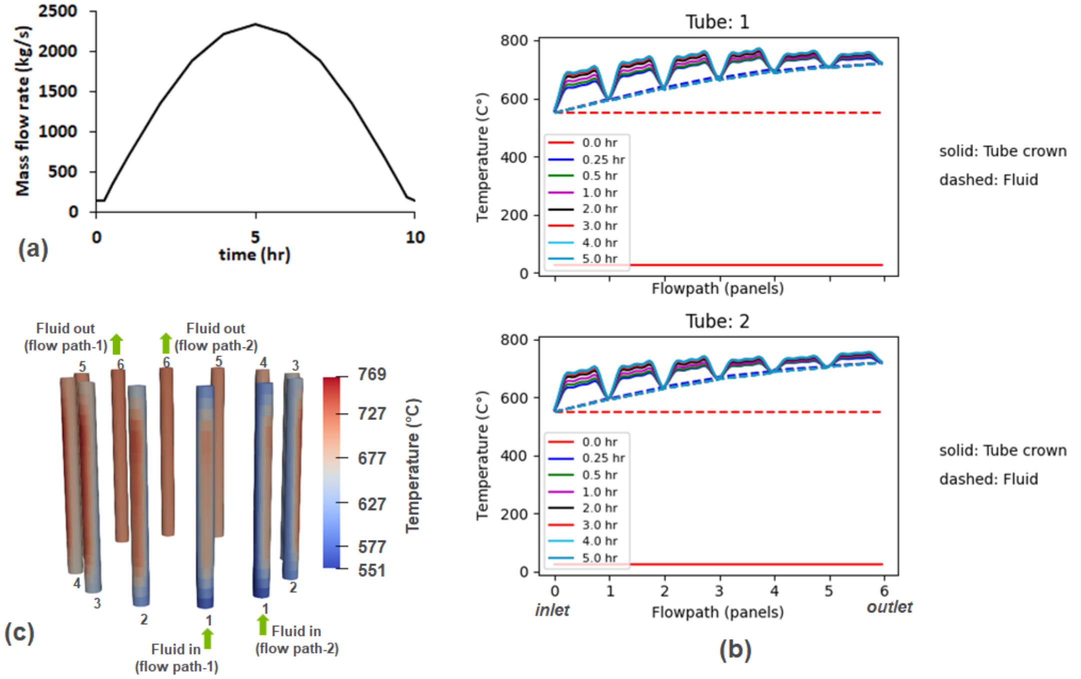

Figure 5.2. (a) Variation in fluid mass flow rate, optimized to achieve nearly constant, 720°C outlet temperature. (b) Changes in fluid and tube crown temperatures (shown for two representative tubes per panel considered in simulation) along the flow path from the start of the day to noon. (c) Tube outer wall temperature distribution (shown for Tube-1) at noon. Results are from thermohydraulic analysis of the reference receiver considering SiC as the tube material and for 1 mm thick tubes. Numbers 1 to 6 indicates the panels in the receiver along two flow paths.

5.3 Structural analysis

We performed structural analysis of the reference receiver using the tube temperature distributions determined in the thermohydraulic analysis and under a design fluid pressure. The design fluid pressure was determined based on the frictional pressure loss between the inlet and outlet at the maximum mass flow rate and head loss due to the height of the receiver (i.e., tube length). Since the frictional pressure loss depends on the fluid velocity, the design pressure depends on the thickness of the tube. The design fluid pressures are 2.2 MPa, 2.6 MPa, and 3.2 MPa for 1 mm, 2 mm, and 3 mm thick tubes, respectively. For structural analysis we considered the tubes in a panel as rigidly connected to the tube manifold but the panels are mechanically disconnected from each other. Previous work [6] on metallic receivers indicates that structural analysis considering the hottest and coldest tubes in a panel provides a conservative estimation of the life of the receiver. Therefore, the structural analysis here considers only the hottest and coldest tubes in the panel.

Figure 5.3 shows results from structural analysis of the reference receiver considering SiC as the tube material and 1 mm tube thickness. We considered a linear elastic model to represent the deformation of SiC. The contour plots of different stress components in Figure 5.3 indicate the axial (zz) stress component is significantly higher than the other two stress components. This is expected as the tubes are subjected to axial constraint by the tube manifold as well as axial bending due to the circumferentially large temperature difference. An important observation from the analysis is that the high stress locations in the tubes are mostly in compression. This has a significance in selecting a failure model for ceramic receiver design as ceramic materials are much stronger in compression than tension. A model that does not distinguish between tensile and compressive stresses will more likely predict much lower reliability for ceramic receivers than models that do.

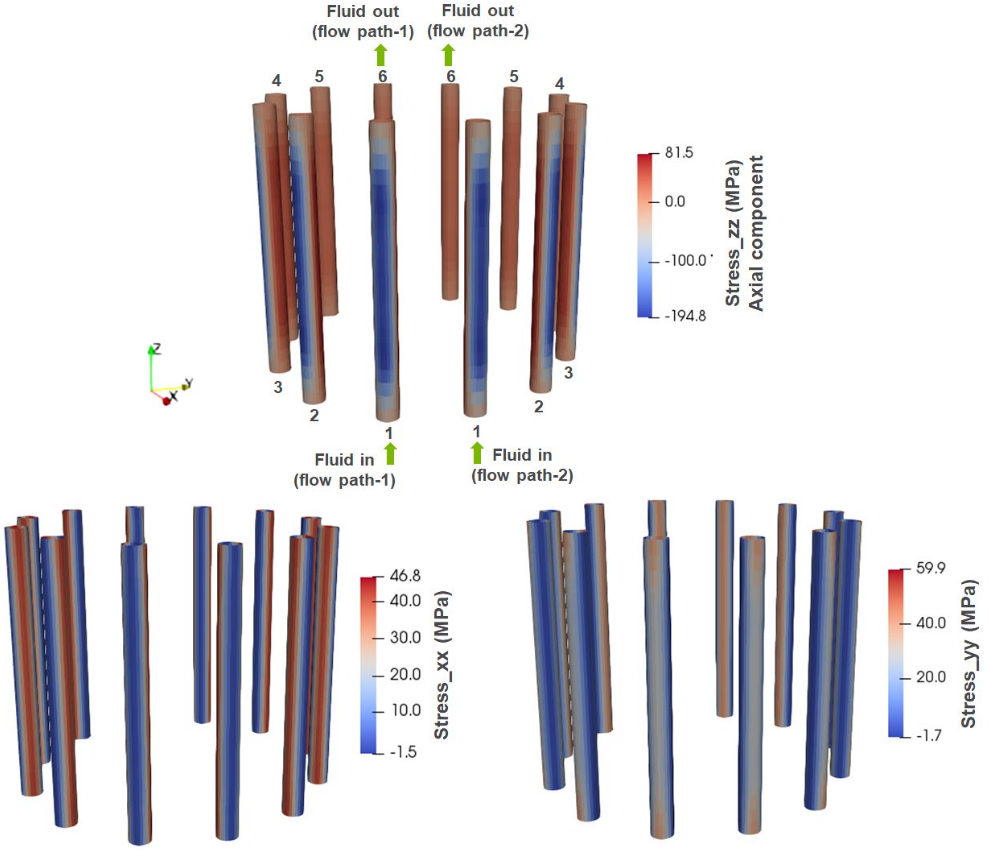
Fluid out
(flow path-1)
Fluid out
(flow path-2)
4
5
6
6
5
4
3
2
1
1
2
3
Fluid in
(flow path-1)
Fluid in
(flow path-2)
Z
Y
X
81.5
0.0
-100.0
-194.8
Stress_zz (MPa)
Axial component
46.8
40.0
30.0
20.0
10.0
-1.5
Stress_xx (MPa)
59.9
40.0
20.0
-1.7
Stress_yy (MPa)

Figure 5.3. Stress distributions (shown for Tube-1) at noon. Results are from structural analysis of the reference receiver considering SiC as the tube material and for 1 mm thick tubes. Numbers 1 to 6 indicates the panels in the receiver along two flow paths.

5.4 Reliability analysis

We performed reliability analysis of the reference receiver for two ceramic materials – SiC and Ti_3SiC_2 MAX Phase. Reliability analysis requires the m and σ_0 Weibull coefficients for the material for all the failure models. The SMM models requires an additional parameter, $\bar{C}$ which is the ratio of the critical value of Mode II stress intensity factor, K_{II} in pure Mode II loading the Mode I fracture toughness, K_{IC}. Determining the value of $\bar{C}$ requires performing fracture tests in mixed mode conditions which is beyond the scope of the project. To be able to use the SMM models, we considered $\bar{C} = 1.5$, a value in the range of $0.8 \leq \bar{C} \leq 2.0$ found by Shetty [14] for ceramic materials. Table 5.1 lists the material parameters used in reliability analysis of SiC and Ti_3SiC_2 MAX Phase tubes.

Note Table 5.1 lists two sets of parameters for SiC – one from literature and one determined from the experiments conducted as part of this project. There is a significant variation in the material parameters between the SiC (literature) and SiC (tested). Specifically, the low value of m for SiC (tested) indicates significant variation in the tested sample which may result in very low reliability of the receiver tubes.

Also note that the parameters for Ti_3SiC_2 MAX Phase at 800°C are based on only four tests – two conducted at 800°C and two conducted at 900°C – and therefore the variability in the material strength might not be captured entirely.

Table 5.1. Material parameters used in reliability analysis.

	Temperature (°C)	Weibull modulus, m	Scale parameter, σ_0 (MPa-(mm)^(3/m))	Mixed mode constant, $\bar{C}$
SiC (literature) [29]	25	10.70	507	$1.5^{\&}$
	800	10.70	467	$1.5^{\&}$
SiC (tested)	25	7.38	411	$1.5^{\&}$
	$800^{\$}$	6.97	419	$1.5^{\&}$
Ti_3SiC_2 MAX Phase	25	36.26	528	$1.5^{\&}$
	$800^{\#}$	25.34	489	$1.5^{\&}$

$^{\$}$ parameters are based on tests performed at 750°C. $^{\#}$ parameters are based on only 4 tests: two at 800°C and two at 900°C. $^{\&}$ a random value selected based on $0.8 \leq \bar{C} \leq 2.0$ for ceramic materials.

Using the stress results from the structural analysis, *srlife* performs the reliability analysis by calculating the reliability at each time step using the ceramic failure model selected by the user. At the end of the analysis, *srlife* provides the reliability for individual tubes considered in analysis. As discussed above, the current ceramic failure models implemented in *srlife* are time-independent models. The individual tube reliability, therefore, is the minimum reliability during the load cycle considered. Note following the CARES manual *srlife* assigns a reliability of 1 to the elements with minimum principal stress larger than three times the maximum principal stress.

The bar chart in Figure 5.4 shows the reliability of individual tubes considered in the analysis based on the PIA model. These results are for 1 mm thick tubes and considering SiC (literature) as the receiver material. The minimum value of the individual tube reliabilities then can be used as the measure of the reliability of the receiver tubes.

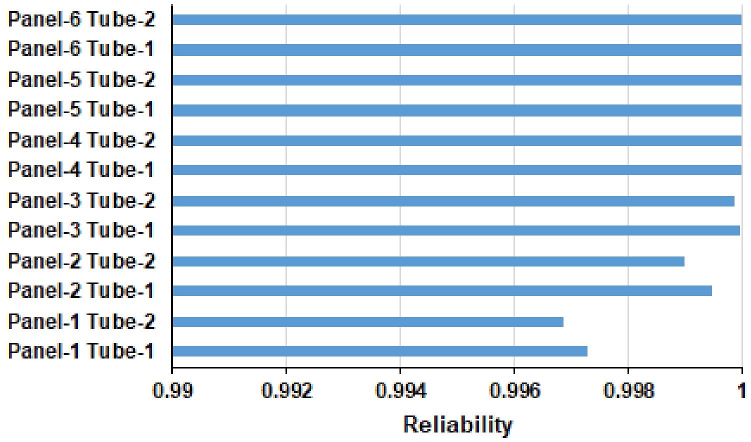

Figure 5.4. Individual tube reliabilities of the reference receiver using PIA model. Tube material: SiC (literature) and tube thickness: 1 mm.

5.4.1 *Reliability vs failure models*

We assessed the ceramic failure models in terms of their conservatism and applicability for high temperature receiver. Figure 5.5 compares the minimum tube reliability of the reference receiver, considering SiC (literature) as the tube material and 1 mm thick tubes, computed using different failure models discussed above. The figure ranks the model in the following order in terms of their conservatism in calculating reliability of receiver tubes:

PIA < WNTSA < MTS_GF < MTS_PSF < SMM_GF < SMM_PSF< CSE_GF < CSE_PSF

This order is different than the order found for the transversely loaded circular disc example problem in CARES manual. The SMM models, as discussed above, calculate the least reliability for the circular disc problem, while the CSE models calculate the least reliability for the receiver tubes. We believe this is due to an inherent flaw in the CSE models. The effective stress (Eq. 2.21 and Eq. 2.22) formulations in the CSE models are agnostic towards the type of stress, as it is always calculated on positive values of the normal and shear stresses, even if the stresses are compressive in nature. As indicated by Figure 5.3, the receiver tubes experience compressive stresses at many locations and therefore CSE models calculate much lower reliability than other models. We therefore do not recommend CSE models for reliability assessment of receiver tubes. Among other models the SMM models are the most conservative. However, reliability assessment using SMM models requires an additional material parameter, $\bar{C}$ which can be determined only from biaxial tests. If the value of $\bar{C}$ is not available for a material, designers may try different values of $\bar{C}$ in the range $0.8 \leq \bar{C} \leq 2.0$ and report both the least and most conservative estimations of reliability. Designer may avoid using SMM models if $\bar{C}$ is not available. In that case, the MTS_PSF model would provide the most conservative estimation of reliability.

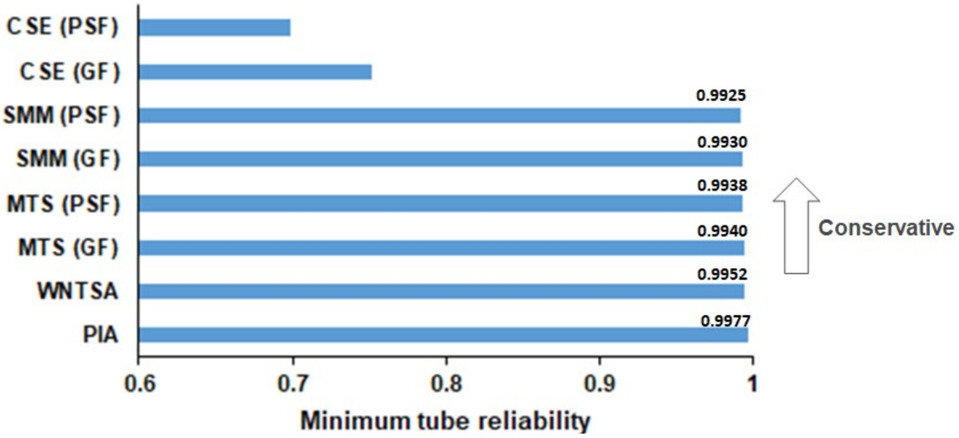

Figure 5.5. Minimum tube reliability vs ceramic failure model. Tube material: SiC (literature) and tube thickness: 1 mm.

5.4.2 Reliability vs tube thickness

Additive manufacturing techniques are expected to be used to manufacture the ceramic receiver tubes. The current 3D printed sintered ceramic tubes at ANL (as part of another project) are thicker than 1 mm. This requires assessment of the reference receiver for different tube thicknesses. Figure 5.6 compares the minimum tube reliability for different tube thickness. The figure indicates reduction in reliability as tube thickness increases. With the increase of tube thickness the primary stresses reduce but the secondary stresses increase due to higher through thickness thermal gradient. Since the pressure load is significantly less than the thermal load for this reference (chloride salt) receiver, the reduction in primary stresses with thickness increase is not as significant as the increase in thermal stresses and hence lower reliability. An opposite trend might be possible for receivers that operate using high pressure HTF such as sCO_2.

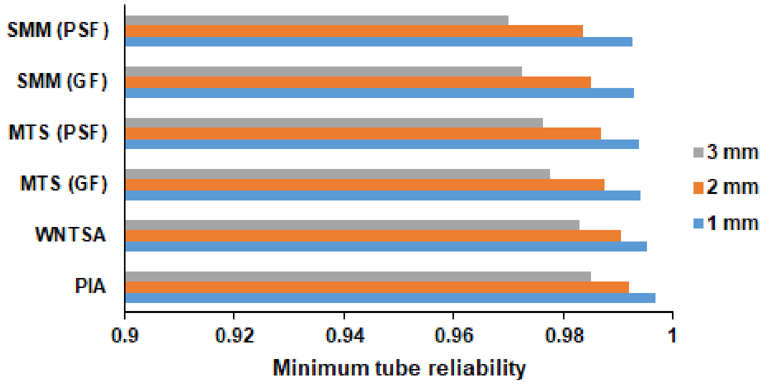

Figure 5.6. Minimum tube reliability vs tube thickness. Tube material: SiC (literature).

5.4.3 Reliability vs materials

Figure 5.7 compares the reliability of the reference receiver with 3 mm thick tubes for different tube materials: SiC (literature), SiC (tested), and Ti_3SiC_2. The reliability for Ti_3SiC_2 tubes is always 1 irrespective of the failure model. The reliability of SiC (literature) tubes is in between 0.97 and 0.99 depending on the type of failure model is used. The SiC tested as part of this project exhibits near zero reliability for all the failure models. As discussed above, the *m* value for this SiC is very low (~ 7) which indicates large variability in the material's strength and therefore tallies probability of failure even at very low stress values. We plan to purchase SiC with higher *m* value for next year's test campaign examining time-dependent properties.

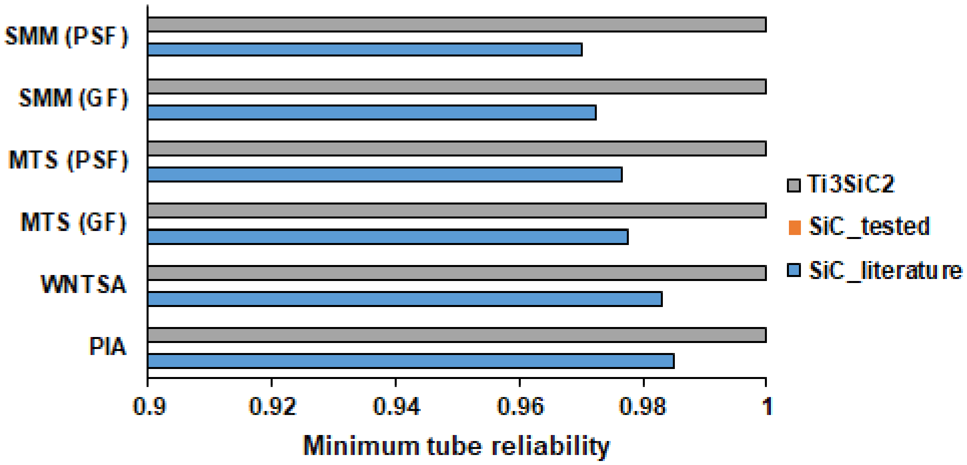

Figure 5.7. Minimum tube reliability vs tube material. Tube thickness: 3 mm. The bar for SiC (tested) is not visible because tube reliability for this material is about zero for all the models.

5.5 Comparison with metallic receivers

Finally, the viability assessment of ceramic materials for high temperature receiver must include a comparison between ceramic and metallic receivers. However, there is no easy way to compare these two material groups as the failure criteria are very different. For metallic receivers, we can directly estimate the life of the receiver by calculating the creep-fatigue damage accumulation for each load cycle. Life estimation is not possible for ceramic receivers, rather a check on the target reliability can be performed. Selecting the value of target reliability depends on many factors such as availability of the experimental data from similar parts/components, consequences of failure of the actual component, etc. To the best of our knowledge, there is no such failure data available for ceramic tubes subjected to solar incident as well as internal fluid pressure. Failure data for different type of components are available in literature. For example, proof tests of the ceramic turbine wheels of Marcedes-Benz research car 2000 [30] showed a time-independent reliability of 0.87 – 0.98.

Table 5.2 lists the estimated life of the reference receiver for two high temperature nickel based metallic alloys and the reliability of the receiver for two ceramic materials. Note the tube thickness is 1 mm for the metallic receivers and 2 mm for the ceramic receivers. The difference in tube thickness between two types of materials is based on the most optimum design as well as the viability of manufacturing of such tubes. For the ceramic materials, the table lists reliability using MTS (PSF) model because this model, as discussed above, provides the most conservative estimation after the SMM models. SMM models require the value of $\bar{C}$ which is not available. The table indicates estimated life of the metallic receiver is 44 days for A740H and 96 days for A282, while the reliability of ceramic receiver is above 0.98 for both SiC (literature) and Ti_3SiC_2 MAX Phase.

The expected life of the metallic receivers is very short, in line with past estimates of the expected operating life of Ni-based superalloy receivers operating in these high temperature conditions. By contrast, the time-independent reliability of the ceramics is excellent – especially as the metallic life predictions here use best-estimate material properties and so might reasonably represent a median life estimate corresponding to a reliability of 0.5. While a comprehensive assessment will require time-dependent ceramic failure data and corresponding failure models, this initial assessment suggests that high temperature ceramics may make tubular sCO_2 and molten salt receivers viable for designs with >700° outlet temperatures.

Table 5.2. Comparison between metallic and ceramic receivers.

	A740H 1 mm thick tubes	A282 1 mm thick tubes	SiC (literature) 2 mm thick tubes	Ti_3SiC_2 2 mm thick tubes
Life (criteria: creep-fatigue)	44 days	96 days	-	-
Time-independent reliability (Model: MTS_PSF)	-	-	0.987	1.000

6 Conclusions

This report describes the extension of the open-source CSP component design and analysis program *srlife* to analyze and evaluate components constructed from engineering ceramics. The current report describes the first year of progress on this project which focuses on time-independent ceramic failure. The key activities in this first year were:

1. We modified the software tool *srlife* to analyze time-independent, high temperature ceramic failure. These models were mostly developed through past work at NASA. We verified our implementation of the models by direct comparison to simulation results from the CARES/LIFE program, developed by NASA, reported in the CARES/LIFE manual.
2. We added a thermohydraulics solver to *srlife* to allow us to make a fair comparison between equivalent metallic and ceramic receiver designs.
3. We collected the data required to parameterize the time-independent failure models for commercially-obtained SiC. This required completing a test matrix of high and room temperature bend tests on samples of the material and postprocessing the data to obtain Weibull statistics for this batch of SiC.
4. We supplemented the SiC test data with data obtained from the literature on other batches of commercial SiC and with Ti_3SiC_2 MAX Phase data collected as part of another DOE-sponsored project.
5. We then used the new capabilities in *srlife* and the test data to analyze prospective ceramic solar receiver designs, using both MAX phase and commercial SiC material. We compared the results of these analyses to comparable analyses of equivalent metallic receiver designs using Ni-based superalloy materials.
6. We placed a long lead time order for a creep frame capable of high temperature bend tests on ceramic materials. This will be a critical piece of equipment for phase II of the project.

Our recommendations and conclusions, based on this work, are:

1. High temperature ceramic receivers are viable and should be explored further.
2. Proceed to the second phase of the project looking at time dependent ceramic failure using commercial SiC as the target material. The second phase of the project will develop models for time-dependent ceramic failure and collect the required time-dependent failure data to support the models. While the MAX phase materials may be somewhat stronger at the relevant temperatures, difficulty in obtaining repeatable material samples would likely slow or prevent completion of the required high temperature, time-dependent testing.
3. As a general recommendation, we suggest using the Griffith's maximum tensile stress (MTS) criteria assuming a penny-shaped flaw for time-independent analysis of ceramic receivers.

Acknowledgements

This work was sponsored by the U.S. Department of Energy, under Contract No. DE-AC02-06CH11357 with Argonne National Laboratory, managed and operated by UChicago Argonne LLC. Funding was provided by the U.S. Department of Energy, Office of Energy Efficiency and Renewable Energy, Solar Energy Technologies Office, Concentrating Solar Power Program, under award #38482.

Bibliography

[1] Mehos, Mark, et al. “Concentrating Solar Power Gen3 Demonstration Roadmap.” National Renewable Energy Laboratory technical report, NREL/TP-5500-67464 (2017).

[2] Barua, B., M. C. Messner, and M. D. McMurtrey. "Comparison and Assessment of the Creep-Fatigue and Ratcheting Design Methods for a Reference Gen3 Molten Salt Concentrated Solar Power Receiver." ASME 2019 Pressure Vessels and Piping Conference (2019).

[3] Ghavam, Seyedehhoma, Maria Vahdati, I. A. Wilson, and Peter Styring. "Sustainable ammonia production processes." *Frontiers in Energy Research* (2021): 34.

[4] Kim, Jinsoo, Benjamin K. Sovacool, Morgan Bazilian, Steve Griffiths, Junghwan Lee, Minyoung Yang, and Jordy Lee. "Decarbonizing the iron and steel industry: A systematic review of sociotechnical systems, technological innovations, and policy options." *Energy Research & Social Science* 89 (2022): 102565.

[5] Messner, M. C., B. Barua, and Dileep Singh. “Towards a Design Framework for Non-metallic Concentrating Solar Power Components.” SolarPACES Conference (2020).

[6] Messner, Mark C., Bipul Barua, and Michael McMurtrey. srlife: A Fast Tool for High Temperature Receiver Design and Analysis. No. ANL-22/29. Argonne National Laboratory (2022).

[7] Nemeth, Noel N., Lynn M. Powers, Lesley A. Janosik, and John P. Gyekenyesi. *CARES/LIFE ceramics analysis and reliability evaluation of structures life prediction program*. No. NASA/TM-2003-106316 (2003).

[8] R. L. Barnett, P. C. Hermann, J. R. Wingfield, and C. L. Connors, “Fracture of Brittle Materials Under Transient Mechanical and Thermal Loading,” (1967).

[9] Freudenthal and A. M., “Statistical approach to brittle fracture,” *Fract. An Adv. Treatise*, II, pp. 591–619, (1968).

[10] Weibull, W., “A statistical theory of strength of materials,” *IVB-Handl.*, (1939).

[11] B. Gross and J. P. Gyekenyesi, “Weibull Crack Density Coefficient for Polydimensional Stress States,” *J. Am. Ceram. Soc.*, vol. 72, no. 3, pp. 506–507, (1989).

[12] Batdorf, S. B. and H. L. Heinisch. “Weakest Link Theory Reformulated for Arbitrary Fracture Criterion,” *J. Am. Ceram. Soc.*, vol. 61, no. 7–8, pp. 355–358, (1978).

[13] S. B. Batdorf and J. G. Crose, “Statistical Theory for the Fracture of Brittle Structures Subjected To Nonuniform Polyaxial Stresses.,” Am. Soc. Mech. Eng., no. 74-APM-D, (1974).

[14] D. K. Shetty, “Mixed-Mode Fracture Criteria for Reliability Analysis and Design With Structural Ceramics,” vol. 109, (1987).

[15] K. Palaniswamy, “On the Problem of Crack Extension in Brittle Solids under General Loading,” Mech. Today, vol. 4, p. 30, (1978).

[16] A. C. Rufin, D. R. Samos, and R. J. H. Bollard, “Statistical failure prediction models for brittle materials,” AIAA J., vol. 22, no. 1, pp. 135–140, (1984).

[17] ASTM International, “ASTM Standard Test Method for Flexural Strength of Advanced Ceramics at Ambient Temperautre C1161 - 18,” 2003. doi: 10.1520/C1161-18.1.

[18] ASTM International, “ASTM Standard Test Method for Flexural Strength of Advanced Ceramics at Elevated Tempeartures C1211 - 18,” 2003. doi: 10.1520/C1211-18.2.

[19] ASTM C1239, “Standard Practice for Reporting Uniaxial Strength Data and Estimating Weibull Distribution Parameters for Advanced Ceramics,” ASTM, vol. I, no. January, pp. 1–17, (2000)

[20] S. B. Batdorf, “Some approximate treatments of fracture statistics for polyaxial tension,” Int. J. Fract., vol. 26, no. 4, pp. 394–400, (1984)

[21] B. Gross and J. P. Gyekenyesi, “Weibull Crack Density Coefficient for Polydimensional Stress States,” J. Am. Ceram. Soc., vol. 72, no. 3, pp. 506–507, (1989).

[22] G. Ashish, J. Michael, W. Kenneth, K. Albert, and B. Richard, “Journal of the American Ceramic Society - February 1989 - Ghosh - Elevated-Temperature Fracture Resistance of a Sintered .pdf,” J. Am. Ceram. Soc., vol. 72, no. 2, pp. 242–47, (1989).

[23] Bradbury, J. et al. “JAX: composable transformation of Python+NumPy programs.” http://github.com/google/jax (2018).

[24] Gnielinski, Volker. "Neue Gleichungen für den Wärme-und den Stoffübergang in turbulent durchströmten Rohren und Kanälen." *Forschung im Ingenieurwesen A* 41, no. 1 (1975): 8-16.

[25] Xu, Xiankun, Xiaoxin Wang, Peiwen Li, Yuanyuan Li, Qing Hao, Bo Xiao, Hassan Elsentriecy, and Dominic Gervasio. "Experimental test of properties of KCl–MgCl2 eutectic molten salt for heat transfer and thermal storage fluid in concentrated solar power systems." *Journal of Solar Energy Engineering* 140, no. 5 (2018).

[26] Span, Roland, and Wolfgang Wagner. "A new equation of state for carbon dioxide covering the fluid region from the triple-point temperature to 1100 K at pressures up to 800 MPa." Journal of physical and chemical reference data 25.6 (1996): 1509-1596.

[27] https://webbook.nist.gov/chemistry/fluid/

[28] Wagner, Michael J. and Tim Wendelin. “SolarPILOT: A power tower solar field layout and characterization too.” *Solar Energy* 171, pp. 185-176 (2018).

[29] Tanaka, T., Nakayama, H., Sakaida, A., & Imamichi, T. (1995). Evaluation of Weibull parameters for static strengths of ceramics by Monte Carlo simulation. *Journal of the Society of Materials Science, Japan*, *44*(498Appendix), 51-58.

[30] Hempel, H., and H. Wiest. "Structural analysis and life prediction for ceramic gas turbine components for the Mercedes-Benz research car 2000." *Turbo Expo: Power for Land, Sea, and Air*. Vol. 79290. American Society of Mechanical Engineers, 1986.

Applied Materials Division
Argonne National Laboratory
9700 South Cass Avenue, Bldg. 212
Argonne, IL 60439

www.anl.gov

Argonne National Laboratory is a U.S. Department of Energy
laboratory managed by UChicago Argonne, LLC